Evaluation of Geochemical and Reactivity Changes of Different Iron Materials

by

Jin suk O

A thesis
presented to the University of Waterloo
in fulfillment of the
thesis requirement for the degree of
Master of Science
in
Earth Sciences

Waterloo, Ontario, Canada, 2006

© Jin suk O 2006

I hereby declare that I am the sole author of this thesis. This is a true copy of the thesis, including any required final revisions, as accepted by my examiners.

Jin suk O

I understand that my thesis may be made electronically available to the public.

Jin suk O

Abstract

Previous studies have suggested that iron PRBs, receiving high concentrations of inorganic constituents in groundwater, may experience passivation because of the accumulation of inorganic precipitates. In an iron PRB containing more highly reactive material, even though the initial contaminant removal rate is faster than for less reactive material, a faster migration of the contaminant removal front may occur due to the greater reactivity loss, caused by faster accumulation of secondary precipitates. In contrast, an iron PRB containing less reactive material may show a slower accumulation of precipitates, and thus will show a slower migration of the contaminant removal front over time. Thus, it is hypothesized that an iron material having moderate initial reactivity may be more advantageous than material having a higher reactivity in terms of long-term performance. The objective of this study was to test this hypothesis by evaluating the changes of the reactivities of different iron materials in the presence of dissolved $CaCO_3$.

Four different iron materials (Connelly, G-M, Ispat and Peerless) were selected for the column experiments. The changes in reactivities of the iron and formation of secondary precipitates over time were assessed, primarily by the iron corrosion rates, calculated from the hydrogen gas generation rates, by the cis-DCE removal rates and by the alkalinity profiles. The accumulation of precipitates in the four columns caused passivation of the iron. The passivation of the iron in turn resulted in migration of the mineral precipitation fronts as well as profiles of cis-DCE, TCE, VC, alkalinity, Eh, pH, and chloride. Connelly and G-M had longer periods of operation than Ispat and Peerless and thus their performance was the primary test of the hypothesis. G-M iron, which had the higher initial corrosion rate, compared to

Connelly, showed a faster accumulation of precipitates near the influent end. The difference in accumulated precipitates resulted in a difference in the leading edge of the organic profiles and a significant difference in the pattern of passivation, indicating a faster passivation in the region near the influent end for G-M.

Model simulations were performed using the same fitting parameters but with different initial corrosion rate constants to further test the hypothesis. The model provided a reasonable representation of changing reactivities of the columns, being consistent with the observed data. In the simulation for long-term prediction, the cases of higher corrosion rates showed earlier breakthroughs and steeper curves than those of lower corrosion rates. Also, the predictions showed greater porosity loss for the case of higher corrosion rate. Thus, long-term predictions support the hypothesis. Accurate determination of model parameters such as cis-DCE degradation rate constants and iron corrosion rates are required for better predictions of long-term performance.

Acknowledgements

I would like to express my appreciation to my supervisors, Dr. R.W. Gillham and Dr. Gui Lai, for providing me with the opportunity to conduct this research, and for their continuous guidance, affection and encouragement during the course of this study. I would also like to thank my committee member, Dr. S.K. Frape for reviewing my manuscript and guiding me in new directions. I would like to express special thanks to Dr. S. Jeen for providing many insightful advice, answering my questions for modeling and experiment, and reviewing my manuscript. Great thanks go to Wayne Noble for invaluable technical assistance and refreshing humor in the laboratory. Thanks also to Harsha Jadeja, Marek Odziemkowski, Marguerite Greavette, Sue Fisher for their invaluable technical and/or administrative assistance.

To Lorretta, Rodney, Steve, Albanie, Yanqi, Li, Tom, Soo, Jerami, Snezana, June, Pattie, Eva, Tiana, Huipping and the rest of Gillhamites: thank you for being great friends in Great country. I would also like to thank many members of the UW Korean Graduate Student Association and Earth sciences Schist head soccer team for sharing many experiences with me in Waterloo. Special thanks to Sebum, Yonguen, Soonyoung and Youngjin for big smile and many discussion about Earth.

I would like to thank my Dad, Mom, Changsuk, Sukyoung and my lover Nara in Korea and Eun-kyoung, Sara, Jiwoo, my sweetie Michelle in Canada. Foremost, I would like to express special thanks to my wife for her sharing both the hard and the good times with me. Her patience enabled me to complete this work.

Financial support for this research was provided through the NSERC/duPont/ETI Industrial Research Chair held by Dr. R.W. Gillham, OGSST scholarship and University of Waterloo.

Table of Contents

List of Tables

List of Figures

1. Introduction

Granular iron has been shown to successfully degrade a wide range of chlorinated organic compounds and a variety of other reducible contaminants (Gillham and O'Hannesin, 1994; Matheson and Tratnyek, 1994; Agrawal and Tratnyek, 1996; Orth and Gillham, 1996; Devlin et al., 1998; Blowes et al., 2000; Gui et al., 2000). At the present time, granular iron permeable reactive barriers (PRBs) for the remediation of contaminated groundwater have been installed in many countries (EnviroMetal Technologies Inc., 2006). Field evidence from granular iron PRBs has demonstrated that this technology can provide a long-term, low-maintenance solution for groundwater contamination problems (O'Hannesin and Gillham, 1998; Vogan et al., 1999). Although laboratory and field studies have suggested that mineral precipitates can have a negative effect on the performance of iron PRBs (Mackenzie et al., 1999; Köber et al., 2002; Gu et al., 1999; Phillips et al., 2000; Roh et al., 2000), only recently a limited number of studies have begun to quantitatively examine the pattern of mineral precipitates and consequences in PRB performance.

Zhang and Gillham (2005) concluded that carbonate minerals can reduce the reactivity of granular iron, and this reduction in reactivity can have a major effect on the pattern and extent of precipitate formation. The zone of reduced reactivity will migrate over time from the influent end into the PRB. Thus, understanding and quantifying the effects of mineral precipitation on permeability and reactivity of iron materials are very important for evaluating the long-term performance of PRBs. Jeen (2005) conducted systematic column experiments using longer columns over longer periods of time than the experiments reported in Zhang and Gillham (2005). Through these experiments, Jeen (2005) found that migration of the mineral

precipitation front resulted in a more or less evenly distributed porosity loss throughout the columns. The patterns of various organic and inorganic profiles agreed qualitatively with those of the previous study (Zhang and Gillham, 2005).

The chemical reactions and transport processes within reactive barriers are complex interactive processes, and thus to quantify the effects, or to predict future behaviour requires coupled transport and reaction models. In only a few studies, reactive transport and geochemical processes have been combined within predictive models (Blowes and Mayer; 1999, Mayer et al., 2001; Yabusaki et al., 2001; Li et al., 2005). However, these studies did not include the change of the iron reactivity over time, and thus predictions based on these types of models may be limited to the performance of iron PRBs for relatively short periods of time. More recently, Jeen (2005) incorporated the reactivity change into kinetic expressions in the model MIN3P (Mayer et al., 2001). The simulation results reproduced the observations from the column experiments reasonably well and demonstrated the potential predictive capability of the model.

One of the important implications from the results of the modeling study of Jeen (2005) is that iron having moderate initial reactivity may be advantageous compared to iron having higher reactivity for the long-term performance of PRBs. This is because the high initial precipitation rate in the iron having higher reactivity will result in faster accumulation of precipitates, a greater reactivity loss, and thus, faster migration of the contaminant removal front. In contrast, an iron PRB containing less reactive material will show a slower accumulation of precipitates, and thus, slower migration of the contaminant removal front.

The purpose of this research was to investigate and quantify the relationship between mineral precipitation and iron reactivity and to determine if an optimal reactivity could be

identified. This was undertaken in columns containing iron materials with different initial reactivities. For this purpose, laboratory column experiments were carried out using different iron materials and the results were compared with the predictions of the model of Jeen (2005). In addition to providing further insight concerning the predictive capability of the model, the information could be important in selecting materials to be used in construction of PRBs.

1-1. Background

1-1-1. cis-DCE, VC and TCE

Trichloroethene (TCE) has been studied extensively as a target contaminant for the application of granular iron PRBs. There have been fewer studies focused on cis-dichloroethene (cis-DCE) and Vinyl chloride (VC). One of the challenges for granular iron PRBs is to ensure efficient reductive dechlorination not only for PCE and TCE, but also for the intermediates, in particular cis-DCE and VC (VanStone et al., 2004). The U.S. Environmental Protection Agency's drinking water limits for VC and cis-DCE are 2 μg/L and 70 μg/L (U.S. EPA 2006). cis-DCE has been known as a trigger for liver problems and VC is considered to be carcinogenic as well as causing liver problems. As the lesser chlorinated ethenes (especially cis-DCE) may occur as by-products of TCE in weathered plumes, it is important to understand the effect of precipitates on the iron reactivity towards the intermediates and to ensure complete treatment of these compounds. Thus, cis-DCE was selected as the target contaminant for this study. In addition, TCE and VC were introduced occasionally to the two selected columns to examine the passivation of iron materials towards different organic compounds.

1-1-2. Formation of secondary minerals and effect on reactivity of iron

Various secondary minerals precipitate within iron PRBs because of changes in geochemical conditions. Though there are few cases where adverse performance of PRBs have been atributed to precipitate formation, the majority of the PRBs have not been monitored such that precipitate formation can be quantified. Also, most field studies provide relatively short records of performances, generally less than ten years. Therefore, the potential long-term effects of precipitates on PRB performance needs to be elucidated by more sophisticated studies.

It has been shown that the condition of the iron surface and the availability of the iron surface for the reactions may affect overall hydrogeochemistry (Jeen, 2005). Particularly, in a 16-month column experiment, Zhang and Gillham (2005) found that calcium carbonate in the influent solution resulted in the generation of $CaCO_3$ precipitates and a decline in iron reactivity. The results from Jeen (2005) also showed that mineral precipitation caused a decrease in reactivity of the iron, and that spatially- and temporally-varying reactivity loss resulted in migration of the mineral precipitation fronts, as well as other profiles such as TCE, Cr, alkalinity and dissolved iron. Mineral analyses by Jeen (2005) showed that the major reaction products on the iron surfaces were magnetite, maghemite, aragonite, and iron hydroxy carbonate. Because conditions encountered in the columns for this study will be similar to those for Jeen (2005), it is expected that a similar mineral assemblage would appear as reaction products. Therefore, the present study focuses on the extent and rates of precipitation resulting from using iron materials with different initial reactivities.

1-1-3. Reactive transport model

Reactive transport models, coupled with geochemical reactions, have recently been developed (e.g., Blowes and Mayer, 1999; Mayer et al., 2001; Yabusaki et al., 2001). For example, MIN3P (Mayer, 1999) was developed for multi-component reactive transport simulations in variably saturated porous media. MIN3P was used to calculate the amounts of secondary mineral precipitation and to describe the performance of a reactive barrier at Elizabeth City, NC (Mayer et al., 2001).

Jeen (2005) modified MIN3P to incorporate the relationship between the amounts of precipitates and reactivity of the iron. The results from Jeen (2005) suggest that iron material having optimal initial reactivity may be more beneficial in the long-term operation of PRBs than material having higher initial reactivity, due to a slower accumulation of precipitates. Modeling results suggested that initially, a PRB containing material of higher reactivity will show a faster contaminant removal rate. However, over time, higher reactivity of the iron will result in a faster accumulation of precipitates, and thus a greater reactivity loss. In contrast, an iron PRB containing less reactive iron will show a slower accumulation of precipitates, and thus cause a slower migration of the contaminant removal front over time (Fig. 1-1).

In this study, columns were operated using different iron materials in an attempt to test this hypothesis. The model developed by Jeen (2005) was used as a means of extending the results such that the consequences at greater time could be examined.

1-2. Goals and objectives

The goal of this research was to quantify the relationship between mineral precipitation and iron reactivity and to determine the optimal iron reactivity. The specific objectives are as follows:

1) To evaluate changes in iron reactivity over time in the presence of dissolved $CaCO_3$,

2) To obtain optimal iron reactivity which can degrade chlorinated ethenes at a desired rate but results in minimum amounts of precipitation and thus longer-term performance,

3) To evaluate the predictive capability of the modified MIN3P model (Jeen, 2005) for iron materials of differing reactivity, and

4) To apply the model to estimate the longevity of iron PRBs for iron materials of differing reactivity.

These objectives were pursued through laboratory column experiments using iron materials with different initial reactivities. From organic and inorganic profiles, the patterns and migration rates of precipitate fronts were determined to evaluate the effect of different initial reactivities on the changes in organic degradation rates and accumulation of precipitates. The extent of carbonate mineral formation and the effects of these minerals on the performance of the iron were assessed. Observations from the performance of the column experiments were used to test the hypothesis. Comparisons between the laboratory and simulation results were used to evaluate the predictive capability of the model and further to estimate longevity of iron PRBs, considering iron sources with different initial reactivities.

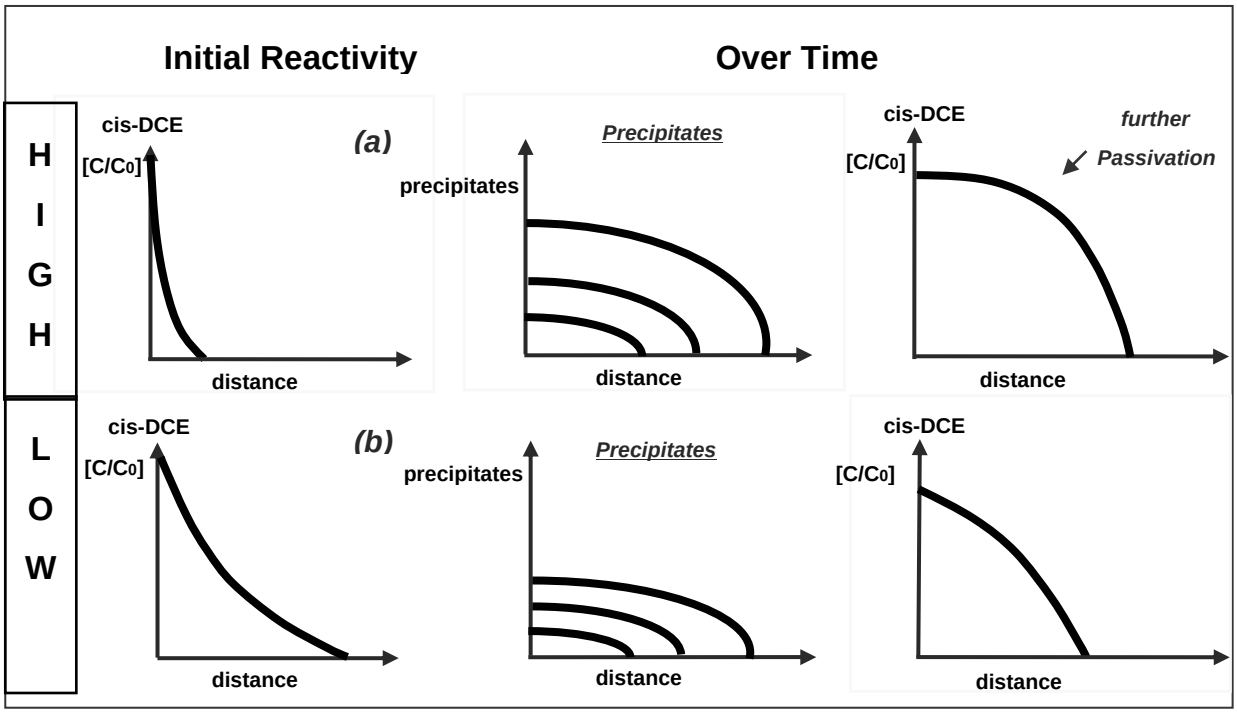

Fig. 1-1. Hypothesis concerning the relationship between precipitate formation and reactivity change: (a) iron with high initial reactivity results in a faster accumulation of precipitates and a greater reactivity loss (b) iron with lower initial reactivity results in a slower accumulation of precipitates and a slower reactivity loss.

2. Methods – Column Experiments

2-1. Experimental design

Four columns, each with a different iron material, were prepared to simulate groundwater flow through iron PRBs. Iron materials were obtained from Connelly (Chicago, IL), Gotthart-Maier (GOTTHART MAIER Metallpulver GmbH), Peerless (Detroit, MI) and Ispat (milled in SOREL, QUEBEC). An identical source solution (10 mg/L cis-DCE + 300 mg/L $CaCO_3$) was introduced into the columns. Periodically, the source solution was changed to 10 mg/L TCE + 300 mg/L $CaCO_3$ or 10 mg/L VC + 300 mg/L $CaCO_3$. Columns containing Connelly and G-M iron were operated for about 8 months and 10 months, respectively, whereas columns containing Peerless and Ispat were operated for about 4 months (Table 2-1).

2-1-1. Columns

A schematic of the column apparatus is shown in Fig. 2-1. The column design was similar to that described in Jeen (2005), except larger in diameter. Each column consisted of a 50 cm long clear Plexiglas™ tube with an internal diameter of 3.81 cm. Nine sampling ports were located at 5 cm intervals along the columns with two additional ports at 2.5 and 7.5 cm from the influent end. Each sampling port consisted of a nylon Swagelok® fitting (0.16 cm OD tube × 0.16 cm NPT male connector) tapped into the column wall. Each fitting held a stainless steel syringe needle (16G11/2) packed with glass wool to prevent fine particulates from clogging the needles. Needle tips were adjusted to the central axis of the column.

All columns were packed dry with the as-received commercial granular iron materials that were sieved to a grain size within the range of 40 – 18 mesh (0.42 – 1mm). The surface area of the iron was measured by the BET method (Brunauer et al., 1938), with values for Connelly, Gotthart-Maier (G-M), Ispat, and Peerless iron of 1.38 ± 0.25 m^2/g, 0.51 ± 0.12 m^2/g, 0.62 ± 0.25 m^2/g and 0.66 ± 0.12 m^2/g, respectively. Particle density was calculated from bulk density and porosity. The average bulk density for each column was 3.24 g/cm^3 for Connelly, 3.59 g/ cm^3 for Gotthart-Maier, 2.92 g/cm^3 for Peerless and 2.34 g/cm^3 for Ispat. The characteristics of each column are summarized in Table 2-1.

In the process of column packing, a coarse Nytex® screen, followed by a fine Nytex® mesh screen, was placed both at the bottom and top to help distribute the flow evenly over each end and to retain fine particles. Each column was packed in about 5 cm lifts and each lift was lightly tamped with an acrylic rod; then the surface was roughened before the addition of the next lift. The initial porosity was determined from the volume of each column, the total mass of iron added, and the column weight measured after saturation of the column with water (using a density of water for 1.0 g/cm^3). The initial porosity calculated for each column is listed in Table 2-1. After filling with iron, the columns were purged with CO_2 gas for about 2 hr, followed by several pore volumes (PVs) of deoxygenated water to ensure complete saturation before feeding the various solutions.

2-1-2. Feed solutions

To prepare the $CaCO_3$ solutions, a pre-calculated amount of analytical grade $CaCO_3$(s) was added to a 22 L glass carboy containing 18 L of de-ionized water. The solution was then

purged with CO_2 gas to dissolve the $CaCO_3$(s) and then the solution was adjusted to pH 6.5 – 6.9. The source solution containing no dissolved $CaCO_3$ was deoxygenated by purging with oxygen-free N_2 gas for about 2 hours. After being purged, the dissolved oxygen concentrations were reduced to below 0.2 mg/L, as measured by CHEMets Kit (K-7501; method detection limit (MDL) of 0.025 mg/L). A concentrated stock solution of cis-DCE, TCE or VC (in methanol) was spiked to the feed solutions to achieve nominal concentrations of 10 mg/L. The feed solutions were refilled every one to two weeks.

Stainless steel tubing was used to connect the glass bottles containing the feed solutions to the columns, to minimize O_2 diffusion, except for short lengths (15 cm) of Ismatec 2-stop Viton® tubing (Cole-Parmer) that passed through the pump. As a further precaution for preventing oxygen intrusion to the bottles, a Mylar™ balloon filled with oxygen-free N_2 gas was connected to a "guard bottle" (Fig. 2-1). The "guard bottle" contained the same solution and the nitrogen gas was equilibrated with the VOC in the solution prior to entering the headspace in the feed bottle. This procedure prevented oxygen contamination of the feed solution and also helped to maintain a relatively constant concentration of volatile organic compounds in the feed solution. The concentrations of VOC and dissolved oxygen, both in the feed and guard bottles, were checked periodically. In the event of a significant decrease in organic concentration or an increase in dissolved oxygen concentration, the solution was replaced.

2-1-3. Column operation

The feed solution was pumped to the bottom (influent) end of the column with a flow rate of approximately 0.4 mL/min using an Ismatec multi-channel peristaltic pump (Model 7619-30). The flow velocity varied between columns as a consequence of differences in porosity, but the initial values were close to 1.0 m/day. Thus, the time to displace one pore volume (PV) of solution was approximately 10 h for Connelly, 12 h for G-M, 16 h for Ispat and 14 h for Peerless. The effluent volume was recorded weekly by weighing the mass of water collected, and the average flow rate during the specific period of time was calculated. The flow rate to the influent end was checked before each sampling event by collecting solution in a graduated cylinder for a fixed time interval. The flow rate measured at the influent end was very similar to that determined from the cumulative effluent.

Teflon® tubing connected to "T" valves near the inlet and outlet of the column were used as manometers (Fig. 2-1) to measure the hydraulic head difference across the column. The hydraulic gradient across the column was calculated from the hydraulic head difference divided by the length of each column, and hydraulic conductivity was calculated from the hydraulic gradient and the solution flux, using the Darcy equation. Therefore, the calculated hydraulic conductivity was an average value across the entire length of the column. The gases emitted from the effluent end were trapped in a sealed glass tube connected in the effluent line (Fig. 2-1). The volume difference in the sealed glass tube over a specific time interval was recorded to estimate the rate of gas generation. The rate of gas production was used to calculate the corrosion rate of the iron in each column.

Solution samples were collected periodically for analyses of organic and inorganic parameters. Samples were collected from each sampling port from effluent end to influent end. After discarding the first few drops of the stagnant solution within the needle, a glass syringe (5, 10, or 20 mL, depending on sampling purpose) was connected to the needle. Sampling was carried out from every week to 2 months for a total of 20 to 30 sampling events for Connelly and G-M and for a total of 9 sampling events for Ispat and Peerless. As shown in Table 2-1, the operating period for the columns varied from about 3 months to 1 year. All experiments were conducted in the same laboratory with an ambient temperature (24 ± 2°C).

2-2. Analytical methods

2-2-1. cis-DCE and VC

Concentrations of cis-DCE and VC as well as the other DCE isomers were determined using a headspace analysis method. A 4 mL aqueous sample was transferred to a 10 mL glass screw-cap vial sealed with a Teflon™-faced butyl-rubber septum. Where concentrations were expected to exceed the calibration range, the sample was diluted 10:1 with distilled water, prior to taking the 4 mL sample for analysis. These sample vials were placed on a rotary shaker for 15 minutes to allow equilibration between the water phase and gas phase, and then placed on a Hewlett Packard 7694 headspace auto-sampler. A 1 mL gas sample was then injected into a Hewlett Packard 5890 Series II gas chromatograph (GC) equipped with an Hnu NSW-PLOT capillary column (15 m × 0.53 mm ID) and an Hnu photo ionization detector (PID) with a lamp potential of 10.2 eV. The initial oven temperature was 50 °C, with a temperature ramp of

20 °C/min to a final temperature of 200 °C, and held for 6 minutes. The detector temperature was 150 °C, and the injector temperature was 100 °C. Ultra pure helium was used as the carrier gas at a flow rate of 20 mL/min. The injector split was 6:1. The method detection limits (MDLs), determined in accordance with the U.S. EPA procedure (U.S. EPA, 1982), were 1.3 μg/L for cis-DCE, and 1.3 μg/L for VC.

2-2-2. TCE

TCE was analyzed using a liquid-liquid pentane extraction method (U.S. EPA, 1979). Two mL of pentane with an internal standard of 500 μg/L of 1,2-dibromoethane was transferred to a 5 mL glass vial with a Teflon™-faced septum screw cap, followed by 1 mL of sample. The internal standard was used to check the concentration of injection volumes on the gas chromatograph. The sample vial was shaken for 15 minutes at 300 rpm on a rotary shaker to obtain equilibration between the water and pentane phases. About 1 mL of pentane was then removed, placed in a 2 mL glass crimp-top GC vial, and placed on a Hewlett Packard 5890 Series II gas chromatograph equipped with a ^{63}Ni electron capture detector (ECD). Using an HP 7673 liquid auto-sampler, a 1 μL sample was injected into a DB-624 capillary column (J&W Scientific; film thickness 3 μm, 30 m × 0.538 mm ID). The detector temperature was fixed to 300 °C, the injection temperature was 200 °C, and the column temperature ramp was 50 °C - 150 °C at a rate of 15 °C/min and held for 1 minute. The carrier gas was pre-purified helium with a total flow rate of 25 mL/min, and the make-up gas was 5% methane/95% argon. The calibration range was from 10 to 3500 μg/L. Samples with concentrations above the calibration range were reanalyzed using a smaller volume of aqueous sample and thus a greater

dilution. Standard solutions of TCE were run daily, before and after each set of samples, to ensure quality of the analysis. The MDL was 1.0 μg/L, determined in accordance with the U.S. EPA procedure (U.S. EPA, 1982).

2-2-3. Chloride, Eh and pH

Chloride analysis, using an Ion Chromatograph (Dionex, Sunnyvale, CA) was conducted for all sampling events. After headspace analysis for the chlorinated organics, 0.5 mL samples were removed and added to 0.5 mL plastic Dionex IC auto-sampler vials. The sample vials were then placed on a Dionex AS-40 auto-sampler. A 25 μL sample was then injected onto a Dionex ICS-2000 Ion Chromatograph equipped with an Ion-Eluent Generator and a conductivity detector. A Dionex IonPac AS18 column (4 × 250 mm) was used. The mobile phase was 30 mM KOH at a flow rate of 1.2 mL/min. The chromatograph was obtained on a Dell p4-3GHz computer using Dionex Chromeleon 6.5 software. The MDL for chloride was 0.5 mg/L.

The oxidation-reduction potential (ORP) was measured with a Markson™ Model 90 digital pH/mV/Temperature meter using a combination Ag/AgCl reference electrode with a platinum redox sensor. The measured potential reading was corrected with respect to standard hydrogen reference electrode (SHE), giving an Eh value, using the standard potential of the Ag/AgCl electrode at the temperature of measurement. Before analyzing samples, the initial electrode response was checked using a standard ZoBell solution (Zobell, 1946; Nordstrom, 1977). The difference between the potential of the Zobell solution relative to the standard hydrogen electrode (SHE) and the measured ORP value of a Zobell solution was added to the

measured ORP values of the samples and thus corrected ORP values represented Eh values. About 3 mL of aqueous sample was collected from a sampling port and was immediately placed in a 5 mL glass vial. The potential reading was recorded immediately when the electrode equilibrated with the solution.

After Eh measurement, the pH of the same sample was measured using a combination glass-Ag/AgCl reference electrode (Orion, Model 91-06) and a Markson™ Model 90 digital pH/mV/Temperature meter. Prior to pH measurement, the electrode response was calibrated with pH buffers. A two-point linear calibration was carried out using a pH 7.0 buffer and either a pH 4.0 or a pH 10.0 buffer, depending on the anticipated pH range of the sample.

2-2-4. Alkalinity

Three mL of sample was transferred to a 10 or 25 mL beaker depending on the expected alkalinity concentration. After 2 or 3 drops of bromocresol green indicator were added and a magnetic stir bar was inserted, the solution was titrated with standardized sulphuric acid (0.0016 N) to the endpoint of pH = 4.5. The amount of acid added to the solution was then back calculated to total alkalinity and expressed in terms of mg/L of $CaCO_3$, with the following equation:

$$\text{Alkalinity (mg } CaCO_3\text{/L)} = (A \times N \times 50000) / (\text{volume of sample (mL)}) \quad (2\text{-}1)$$

Where A is volume of standard acid used (mL),

N is normality of standard acid (mol/L).

With high pH, particularly in the Ispat iron, significant hydroxide alkalinity was anticipated and were measured with separate samples. After 2 or 3 drops of phenolphthalein indicator were added and a magnetic stir bar was inserted, the solution was titrated with standardized sulphuric acid (0.0016 N) to the endpoint of pH = 8.3. The amount of acid added to the solution was then back calculated to phenolphthalein alkalinity and expressed in terms of mg/L of $CaCO_3$ using eq (2-1).

Table 2-1. Column characteristics.

Column	Connelly	Gotthart-Maier	Ispat	Peerless
Source composition	10 mg/L cis-DCE , 10 mg/L TCE , 10 mg/L cis-DCE + 300 mg/L $CaCO_3$ 10 mg/L TCE + 300mg/L $CaCO_3$, 10 mg/L VC + 300mg/L $CaCO_3$			
Grain size	40–18 mesh (0.1–0.42 mm)			
Surface area (m^2/g)	1.38	0.51	0.62	0.66
Column length (cm)	50			
Internal diameter (cm)	3.81			
Sampling port[a] (cm)	2.5, 5.0, 7.5, 10.0, 15.0, 20.0, 25.0, 30.0, 35.0, 40.0, 45.0			
Mass of iron (g)	1846.4	2045.3	1364.2	1700.6
PV[b] (cm^3)	260.4	284.1	382.3	334.4
Porosity (-)	0.46	0.49	0.66	0.58
Bulk density (g/cm^3)	3.24	3.59	2.34	2.92
Operation period[c]	600 PV (271 Day)	660 PV (325 Day)	143 PV (95 Day)	186 PV (108 Day)

[a]Distance from the influent end.

[b]One pore volume.

[c]PV is based on the measured effluent volume; Day is the actual period of operation.

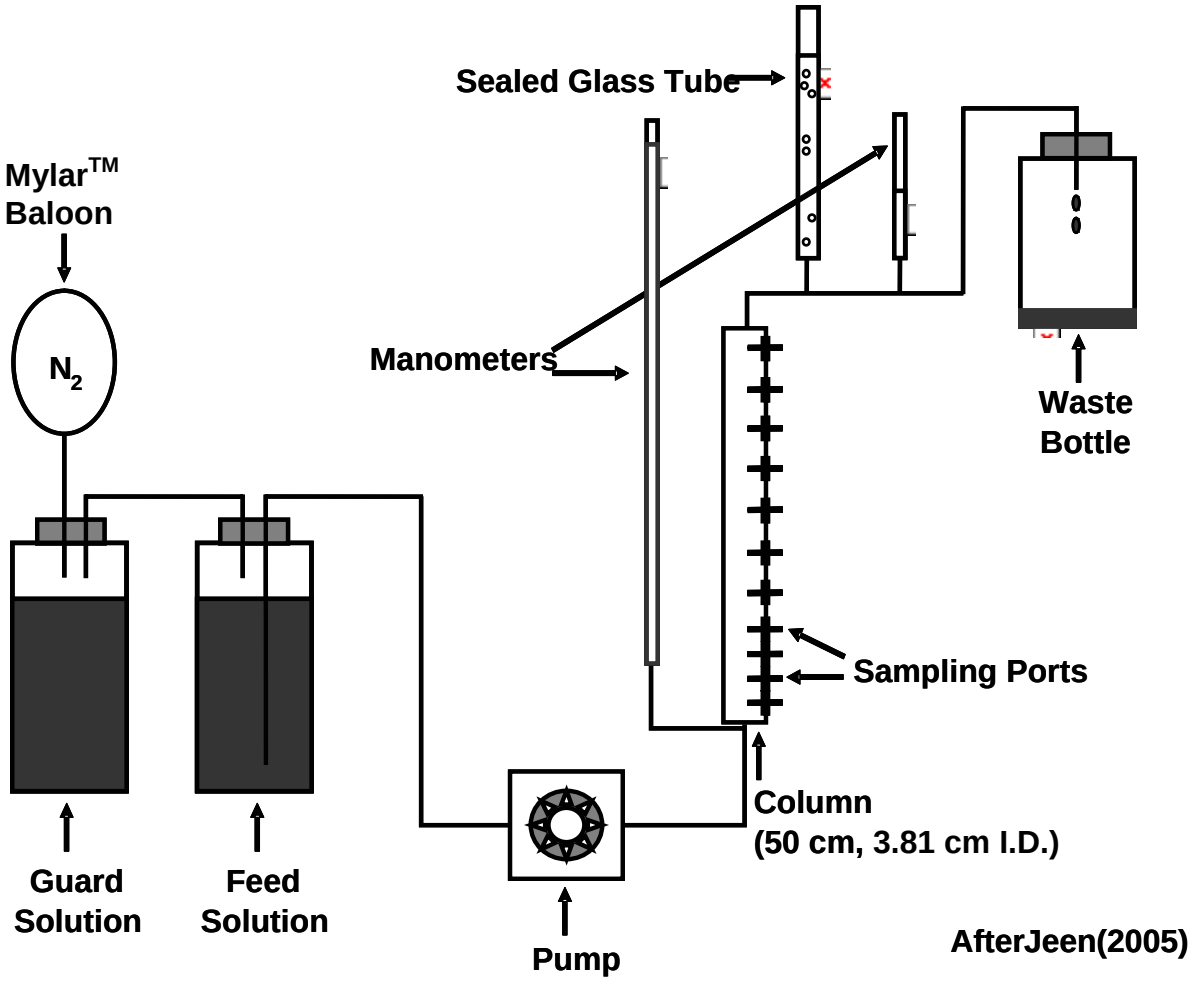

Fig. 2-1. Schematic of column apparatus.

3. Results and Discussion – Column Experiments

3-1. Degradation of chlorinated compounds

Each column received identical source solutions in the following sequence during operation :

(A) 10 mg/L cis-DCE + de-ionized water,

(B) 10 mg/L TCE + de-ionized water (occasional introduction),

(C) 10 mg/L cis-DCE + 300 mg/L $CaCO_3$,

(D) 10 mg/L TCE + 300 mg/L $CaCO_3$ (occasional introduction),

(E) 10 mg/L VC + 300 mg/L $CaCO_3$ (occasional introduction).

(A) and (B) were used to determine the initial reactivity in the absence of $CaCO_3$, (C) was used to evaluate the loss of reactivity toward cis-DCE, as a main target contaminant, in the presence of $CaCO_3$, while (D) and (E) were used to evaluate the loss of reactivity toward other chlorinated ethenes.

3-1-1. Degradation of cis-DCE

As shown in Fig. 3-1, the degradation rates of cis-DCE for G-M, Ispat and Peerless, before $CaCO_3$ addition, were similar, while Connelly iron showed a higher degradation rate than the other three. The cis-DCE profiles for all columns showed a substantial shift toward the

influent end of the columns following introduction of $CaCO_3$, with the exception of Ispat, which showed only a slight shift (Fig. 3-1). The increased reactivity in the presence of HCO_3^- is consistent with results reported by others (Agrawal and Tratnyek, 1996; Gu et al., 1999; Agrawal et al., 2002).

Degradation of chlorinated organic compounds on granular iron has been observed to follow pseudo-first order kinetics with respect to the concentrations of the target organic compounds (e.g., Gillham and O'Hannesin, 1994; Tratnyek et al., 1997; Su and Puls, 1999). The measured concentration data were fitted to the first-order kinetic equation to determine the first-order rate constants ($k_{1,obs}$):

$$\frac{d[\text{cis - DCE}]}{dt} = -k_{1,obs}[\text{cis - DCE}] \qquad (3\text{-}1)$$

where $k_{1,obs}$ is the pseudo-first order rate constant (h^{-1}) and [cis - DCE] is the concentration of cis-DCE. Johnson et al. (1996) introduced a more general expression using the surface area normalized rate constant:

$$\frac{d[\text{cis - DCE}]}{dt} = -k_{SA}\varphi_a[\text{cis - DCE}] \qquad (3\text{-}2)$$

where k_{SA} is the specific reaction rate constant (L H_2O m^{-2} iron h^{-1}) and φ_a is the surface area concentration of Fe^0 (m^2 iron L^{-1} H_2O). This conversion provides a convenient means to compare results from different materials with different surface area, including values reported in the literature.

Table 3-1 shows the initial kinetic parameters calculated by averaging the reaction rate constants for the first two profiles after $CaCO_3$ addition for each column. The surface area concentration of Fe^0 was the greatest (9.80×10^3 m^2 iron L^{-1} H_2O) for Connelly and the smallest (2.21×10^3 m^2 iron L^{-1} H_2O) for Ispat. The calculated k_{SA} values for Connelly, G-M and Peerless are in the same order of magnitude, while the value for Ispat was the lowest. The first two profiles for each column showed the highest reaction rates after $CaCO_3$ addition, and were considered to have reached steady-state before experiencing passivation resulting from mineral precipitation. These profiles were considered to represent the initial (highest) reactivities of the iron in the presence of $CaCO_3$.

Over time, all columns showed migration of the cis-DCE profiles toward the effluent end of the columns (Fig. 3-2), indicating progressive passivation of the iron. Comparing Connelly and G-M (Fig. 3-2 (a) and (b)), the leading edge of the G-M profiles was somewhat further advanced than in the case of Connelly at similar values of PV and there was a significant difference in the pattern of passivation. In the G-M column, there was an expanding zone adjacent to the influent end where there appeared to be little or no degradation, followed by a zone where the rate of degradation was similar, though declining somewhat over time, to the initial rate. In the Connelly material, passivation was expressed as a decline in slope of the degradation curve, starting from the influent end, with only minor evidence of a highly passivated zone immediately adjacent to the influent end. This suggests a greater and faster accumulation of carbonate precipitates in the region close to the influent end for G-M. The operating period for Ispat and Peerless were not sufficiently long to provide clear information concerning the pattern of migration. Nevertheless, the data clearly show migration of the profiles, and suggest patterns more similar to G-M than Connelly (Fig. 3-2 (c) and (d)).

3-1-2. Degradation product (VC)

The only chlorinated product of cis-DCE degradation for all columns was VC and the maximum VC concentration was < 1% of the influent cis-DCE concentration for all columns. The concentration of VC increased with distance along the column as cis-DCE degraded, and then decreased toward the effluent end as VC itself degraded. Fig. 3-3 (a) and (b) shows the VC profiles for Connelly and G-M. At early times, the VC concentration reached a maximum in the regions close to the influent end and then the location of the peak concentration shifted along the column as the experiment proceeded. As expected, the highest VC concentrations were observed in regions where the cis-DCE degradation rates were the highest. The VC profiles reflect higher rate of passivation in G-M than Connelly. For example, the peak of the VC concentration for Connelly at 374 PV was at approximately 12 cm from the influent end, but the peak for G-M at 346 PV was at approximately 20 cm. Though observed over a much shorter period of time, the VC profiles for Ispat and Peerless (Fig. 3-3 (c) and (d)) showed similar behaviour, corresponding to the cis-DCE profiles.

3-1-3. Chloride

Under the assumption of complete degradation of cis-DCE, one mole of cis-DCE should produce 2 moles of chloride. Thus, production of chloride can be used as a supplementary indicator of the extent of the reaction. As the experiment proceeded, the location of the maximum chloride concentration for the four columns migrated further into the

columns, indicating the progression of the passivation front, consistent with the cis-DCE and VC profiles.

Chloride mass balances at various times after $CaCO_3$ addition were calculated and ranged between 85 and 115 %, with no apparent trend with distance along the columns or between the various columns. The cis-DCE and chloride were the major contributors to the total chloride mass balance, with minor contributions from VC.

3-1-4. Degradation behaviour of TCE and VC

For the Connelly and G-M columns, the source contaminant was changed occasionally to TCE or VC to test the passivation behaviour for different organic compounds. The shape and extent of passivation of TCE and VC profiles (Fig. 3-4 (a) and (b)) were similar to that of the cis-DCE profile (Fig. 3-2 (a) and (b)), indicating that the change of surface condition, resulting from mineral precipitation, affects the different chlorinated compounds in a similar manner.

3-2. Corrosion rate

Anaerobic iron corrosion results in the formation of hydrogen, which, in columns containing iron filings, can partition into three phases: gas phase, aqueous phase and solid phase (entrapment of hydrogen in the iron) (Reardon , 1995, 2005). In this study, the H_2 in the gas phase was measured directly by collecting it in a sealed glass tube, assuming that the gas exiting at the effluent end was H_2 only. The H_2 in the aqueous phase was estimated assuming

saturation and using a solubility of 7.515×10^{-4} mol kg^{-1} (for pure water at 100 kPa H_2 at 25°C; Dean, 1992). H_2 in the solid phase was estimated using Sievert's law (Reardon, 1995). The sum of the three phases was used to calculate the corrosion rate, as in Reardon (1995, 2005). The H_2 in the gas phase was the major component, the dissolved H_2 was relatively minor for all columns (about 5 ~ 10 %), and H_2 uptake by the iron contributed to approximately 30 % of the total corrosion rates at early times. However, the contribution of H_2 uptake by the iron for all the columns declined over time. Fig. 3-5 shows the calculated corrosion rates before and after introduction of dissolved $CaCO_3$ for each column. The average iron corrosion rate before introduction of $CaCO_3$ was 0.76 mmol kg^{-1} Fe^0 day^{-1} for Connelly, 0.94 mmol kg^{-1} Fe^0 day^{-1} for G-M, 4.98 mmol kg^{-1} Fe^0 day^{-1} for Ispat and 1.60 mmol kg^{-1} Fe^0 day^{-1} for Peerless, indicating that Ispat and Peerless had significantly higher corrosion rates than Connelly and G-M. After $CaCO_3$ was added, the iron corrosion rate for all four columns increased, particularly for Ispat and Peerless (Fig. 3-5). The maximum values for iron corrosion rates after $CaCO_3$ addition were 3.49 mmol kg^{-1} Fe^0 day^{-1} for Connelly, 4.18 mmol kg^{-1} Fe^0 day^{-1} for G-M, 12.81 mmol kg^{-1} Fe^0 day^{-1} for Ispat and 5.30 mmol kg^{-1} Fe^0 day^{-1} for Peerless. Ispat and Peerless, which had higher initial values, nearly doubled in corrosion rate after introduction of $CaCO_3$. However, the magnitude of the increased iron corrosion rate are not clearly related to the extent of the shifts of the cis-DCE profiles after $CaCO_3$ addition for each column (Fig. 3-1). The extreme case is Ispat, which showed the highest iron corrosion rate after $CaCO_3$ addition but showed the lowest enhancement in terms of cis-DCE degradation. It is possible that excessive hydrogen gas generation of Ispat, for example, could hinder contact of organic contaminant (cis-DCE) with the iron surfaces.

3-3. Formation of precipitates

3-3-1. Visual inspection

The initial and qualitative evidence of precipitate formation was from visual inspection of the columns. The estimated precipitation fronts for Connelly at 85 PV, for G-M at 77 PV, for Ispat at 71 PV, and for Peerless at 80 PV after $CaCO_3$ addition appeared to be located at about 8 cm, 12 cm, 7.5 cm, and 7 cm from the influent ends, respectively. It also appeared that the iron materials having the higher corrosion rates showed a more distinctive grayish white color, particulary near the influent end of the column, with Ispat showing the most distinctive color. Comparing Connelly and G-M, G-M showed a more distinctive grayish white color than Connelly (Fig. 3-6). The precipitation fronts continuously migrated over time, as visually evident in Fig. 3-6 (a) and (b). The precipitation fronts for Connelly and G-M appeared to have migrated to about 38 cm and 48 cm from the influent end at 472 PV and 435 PV after $CaCO_3$ addition, respectively.

3-3-2. Column weight

All columns showed initial decreases in weight prior to $CaCO_3$ addition (Fig. 3-7). The initial weight loss was caused by the accumulation of hydrogen gas within the pore space. Bubbles of H_2 would accumulate in the pore space until a network of continuous gas-filled pores was formed, at which time the continuing production of H_2 would result in the appearance of gas bubbles in the effluent line. At this time, the gas content of the columns

would be expected to be similar to the residual gas phase content of the porous medium. There were considerable difference between columns in the initial weight loss, suggesting differences in the residual gas-phase content. This could be caused by geometric factors such as differences in packing and differences in the geometry of the particles. $CaCO_3$ was introduced to all columns after the column weights reached the lowest levels (Fig. 3-7). The weights of all four columns began to increase after addition of $CaCO_3$ (Fig. 3-7), which are mostly attributed to the accumulation of the precipitates. The slopes of the increases in weight for Connelly and G-M were similar, but with the slope for G-M somewhat greater. The slopes of the increases in weight for Ispat and Peerless were steeper than those for Connelly and G-M, indicating faster accumulation of precipitates due to higher corrosion rate.

3-3-3. Hydraulic conductivity

Hydraulic conductivity was measured over time using the manometers connected to the influent and effluent of the columns. The periodic escape of gases in the effluent line hindered accurate hydraulic head measurements, providing variations and uncertainties in the calculations and thus the degree of scatter is evident in Fig 3-8. The decrease in hydraulic conductivity following addition of $CaCO_3$ was attributed to the accumulation of precipitates. After introduction of $CaCO_3$, the hydraulic conductivity of Connelly and G-M declined approximately one order of magnitude by 500 – 600 PV (Fig. 3-8 (a)). The hydraulic conductivity for Ispat and Peerless decreased to 20 ~ 30 % of the values before introduction of $CaCO_3$ by about 120 PV (Fig. 3-8 (b)). With a longer period of operation and higher $CaCO_3$

concentrations in the influent, Jeen (2005) observed decline in hydraulic conductivity as great as two orders of magnitude.

3-4. Inorganic profiles

3-4-1. Eh

Fig. 3-9 shows the Eh values measured for the four iron materials over time. With $CaCO_3$ addition, the Eh values decreased to approximately -300 mV for Connelly and G-M iron, -400 mV ~ -500 mV for Ispat and -350 mV ~ -390 mV for Peerless throughout the columns. The greatest decrease in Eh values for Ispat agreed well with the highest corrosion rate (Fig. 3-5). The progression of the passivation due to the accumulation of the precipitates caused the Eh values to increase to approximately -100 mV ~ -150 mV for Connelly and G-M, and - 200 mV for Ispat and Peerless at later times.

3-4-2. pH

Fig. 3-10 shows the pH profiles measured at different times for the four columns. With $CaCO_3$ addition, the pH values increased to approximately 9 ~10 for Connelly, G-M and Peerless, and over 10 for Ispat. As passivation of the iron proceeded, the location where pH began to increase migrated further toward the effluent ends of the columns over time. For example, although the first pH profiles after $CaCO_3$ addition for Connelly and G-M showed similar trends, the pH profile for Connelly at 372 PV showed almost constant values at pH 6.8

~ 7.0 up to about 25 cm from the influent end, then gradually increased to pH 9 before reaching the effluent end (Fig. 3-10 (a)), while the pH profile for G-M at 344 PV showed an almost flat value at until 32 cm from the influent and increased to a pH of about 8 before reaching the effluent end (Fig. 3-10 (b)). Ispat showed the highest pH values among all columns (Fig. 3-10 (c)) and this corresponded well with the lowest Eh values (Fig. 3-9 (c)) and highest corrosion rate (Fig. 3-5).

3-4-3. Alkalinity and accumulation of carbonate minerals

As shown in Fig. 3-11, at early times, alkalinity was removed primarily in the region near the influent end of the column, and as the experiment proceeded, the decline in alkalinity occurred further into the columns. It is noted that all columns, except Ispat, had similar alkalinity values at the end of the column throughout the experiments, suggesting that similar amounts of carbonate precipitates should have been accumulated at similar periods of time.

Ispat differed from the other materials in that alkalinity was removed at the highest rate in the region near the influent end, suggesting the fastest precipitation rate resulting from the highest corrosion rate (Fig. 3-5). Compared to the other columns, Ispat iron showed a sharp decrease and a gradual increase from 10 cm from the influent end towards the end of the column, at the same time, it showed the highest pH value toward the effluent end (over pH 10.0, Fig. 3-10 (c)). Thus, in addition to carbonate alkalinity, hydroxide alkalinity was considered to contribute to the measured total alkalinity. When hydroxide alkalinity was measured at 10 PV after $CaCO_3$ addition, hydroxide alkalinity accounted for about 68 mg/L of the total alkalinity of 105 mg/L at the effluent end. For the other three columns, hydroxide

alkalinity did not contribute to the total alkalinity because the pH values were considerably lower (Fig. 3-10 (a), (b), and (d)).

The amounts of the precipitates accumulated along the column over time were calculated from the measured decline in alkalinity. The previous minerals identified in a Connelly iron column operated, under similar geochemical condition, by Jeen (2005) showed that the major carbonate minerals were aragonite ($CaCO_3$) and iron hydroxy carbonate ($Fe_2(OH)_2CO_3$). Thus, it was assumed that the two carbonate minerals were also the major carbonate minerals formed in this study. It was also assumed that the two minerals were formed in an equal molar ratio, as used by Jeen (2005). The total amounts of precipitates accumulated per pore volume was slightly more for G-M iron (0.146 g/PV) than Connelly iron (0.138 g/PV).

3-5. Summary

The accumulation of carbonate precipitates in the four columns (Connelly, G-M, Ispat and Peerless) caused the passivation of the iron over time. The passivation of the iron in turn resulted in the migration of the mineral precipitation fronts as well as the profiles of the cis-DCE, TCE, VC, alkalinity, Eh, pH, and chloride. Between Connelly and G-M, which had the longer periods of operation, G-M iron had the higher initial corrosion rate compared to Connelly iron, and thus potential for faster accumulation of precipitates. After addition of dissolved $CaCO_3$ to the columns, the differences in corrosion rate between the two materials were even greater. The precipitation front for G-M migrated more than the case of Connelly, as observed in visual inspection. The slope of the increase in column weight for G-M was

somewhat steeper than the case of Connelly. The total amounts of precipitates accumulated per pore volume was slightly more for G-M iron than Connelly iron. Thus, the results appeared to support faster accumulation of precipitates for G-M. The leading edge of the G-M profiles was somewhat further advanced than in the case of Connelly, at similar values of PV and there was a significant difference in the pattern of passivation. While G-M iron showed a highly passivated zone adjacent to the influent end, passivation of Connelly appeared more as a decline in slope of the degradation profile, starting from the influent end, with minor evidence of a highly passivated zone. In addition to cis-DCE, the profiles of TCE and VC, supplied as alternate contaminants in the source solution, also showed a similar passivation shape, indicating greater passivation in the region near the influent end for G-M. Therefore, although it is not conclusive with the given data, the experimental data appear to support the hypothesis that iron material having a higher initial reactivity accumulate secondary precipitates faster, particularly in the region close to the influent end, and thus experience faster passivation.

Table 3-1. Initial kinetic parameters for each column treating cis-DCE (10 mg/L) + $CaCO_3$ (300 mg/L).

Column	$k_{1,obs}$ [a] (h^{-1})	$t_{1/2}$ [b] (h)	k_{SA} [c] (L H_2O m^{-2} iron h^{-1})
Connelly	6.4	0.18	6.52×10^{-4}
G-M	2.9	0.24	8.02×10^{-4}
Ispat	0.2	3.46	9.06×10^{-5}
Peerless	1.1	0.61	3.29×10^{-4}

[a]The pseudo-first order rate constant was calculated by averaging the reaction constants for the first two profiles after reaching steady-state in the presence of $CaCO_3$.

[b]Calculated half-life.

[c] $k_{1,obs}$ normalized to the surface area concentration of Fe^0 (m^2 iron L^{-1} H_2O); surface area concentration of Fe^0 for Connelly, G-M, Ispat, and Peerless was 9.80×10^3, 3.61×10^3, 2.21×10^3, and 3.34×10^3 m^2 iron L^{-1} H_2O, respectively.

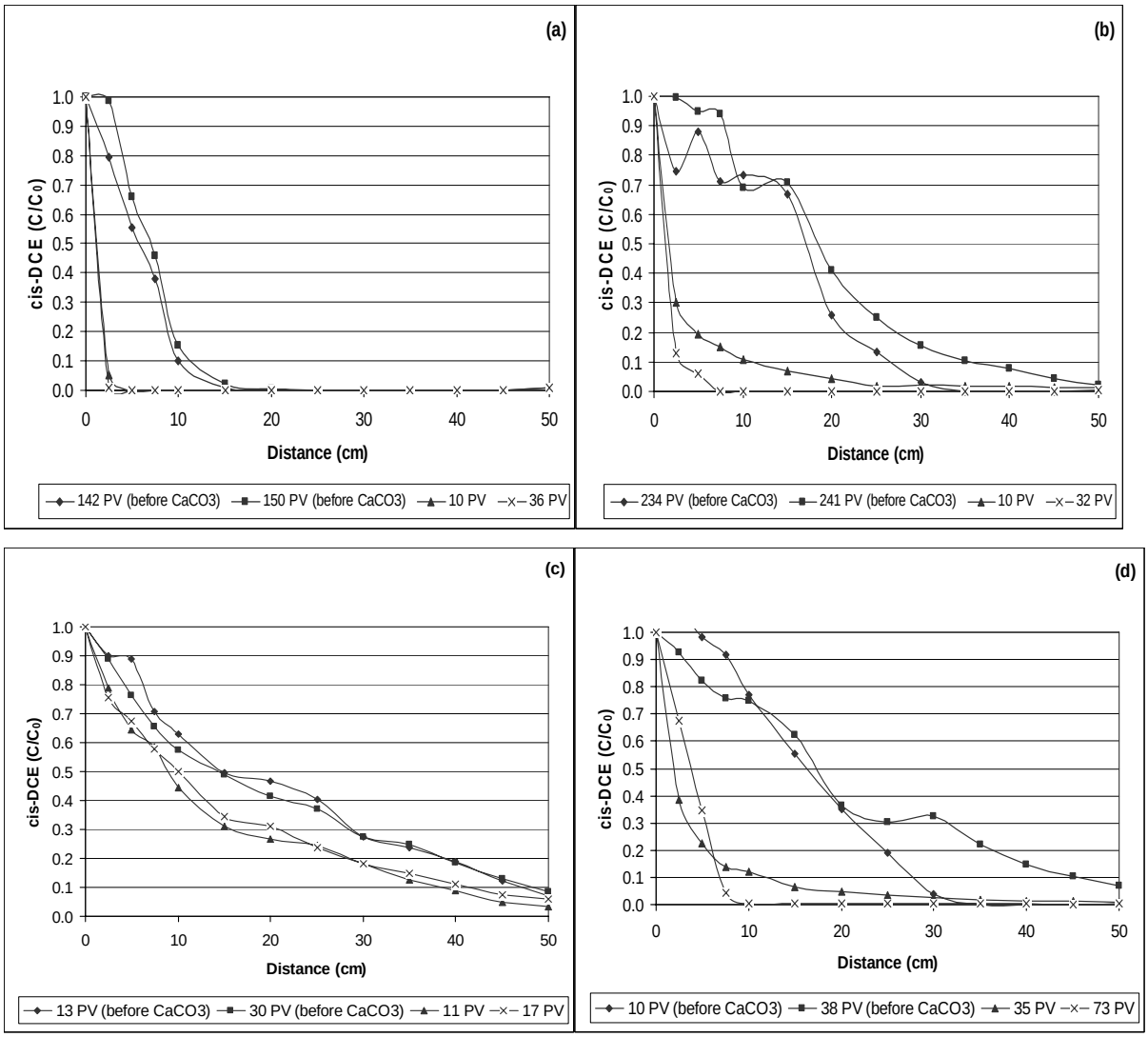

Fig. 3-1. The cis-DCE profiles just before switching to the $CaCO_3$ solution and shortly after $CaCO_3$ addition for (a) Connelly, (b) G-M, (c) Ispat and (d) Peerless iron.

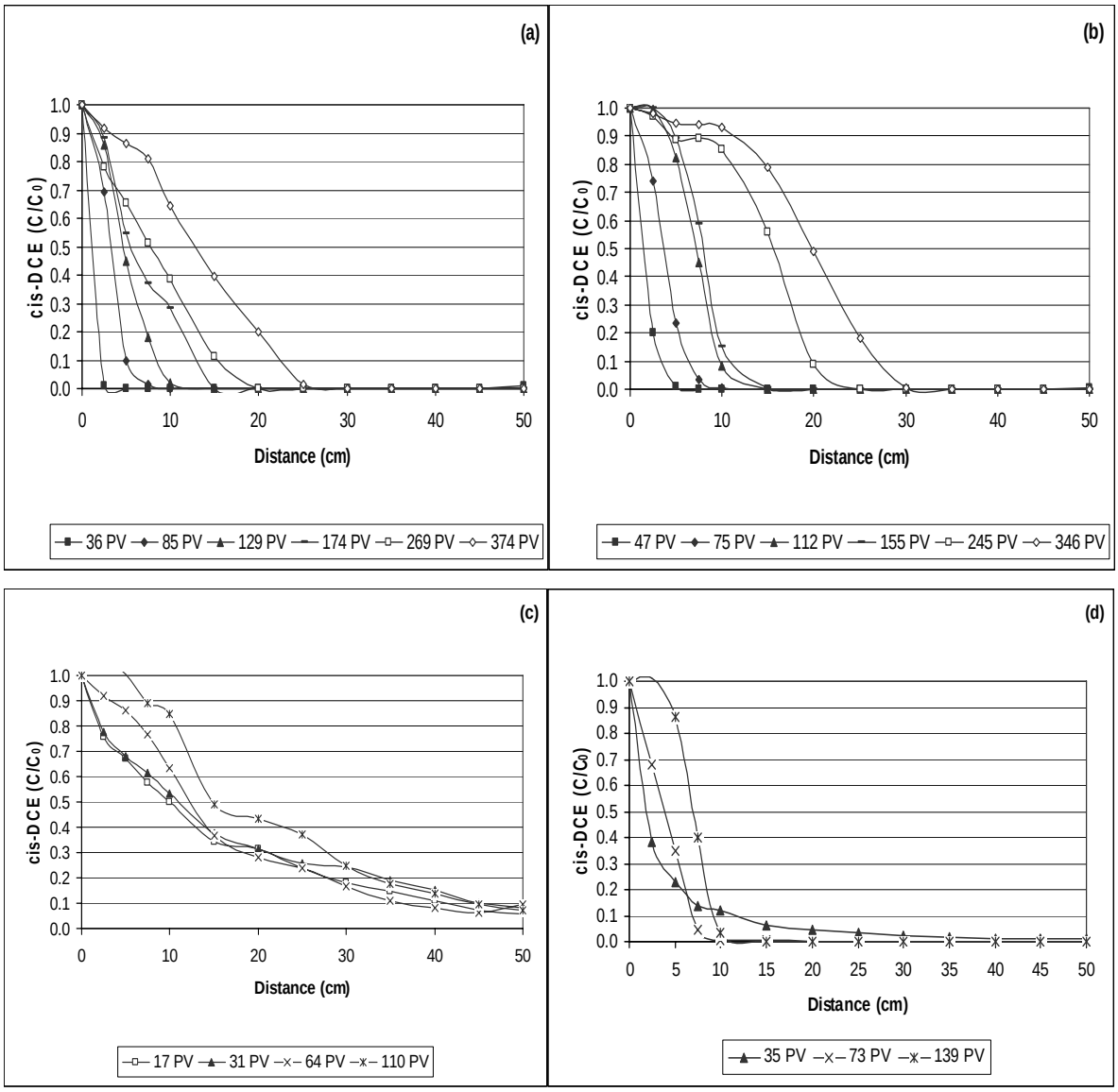

Fig. 3-2. The progression of the cis-DCE profiles after $CaCO_3$ addition for (a) Connelly, (b) G-M, (c) Ispat and (d) Peerless iron. All PV represent pore volume after $CaCO_3$ addition.

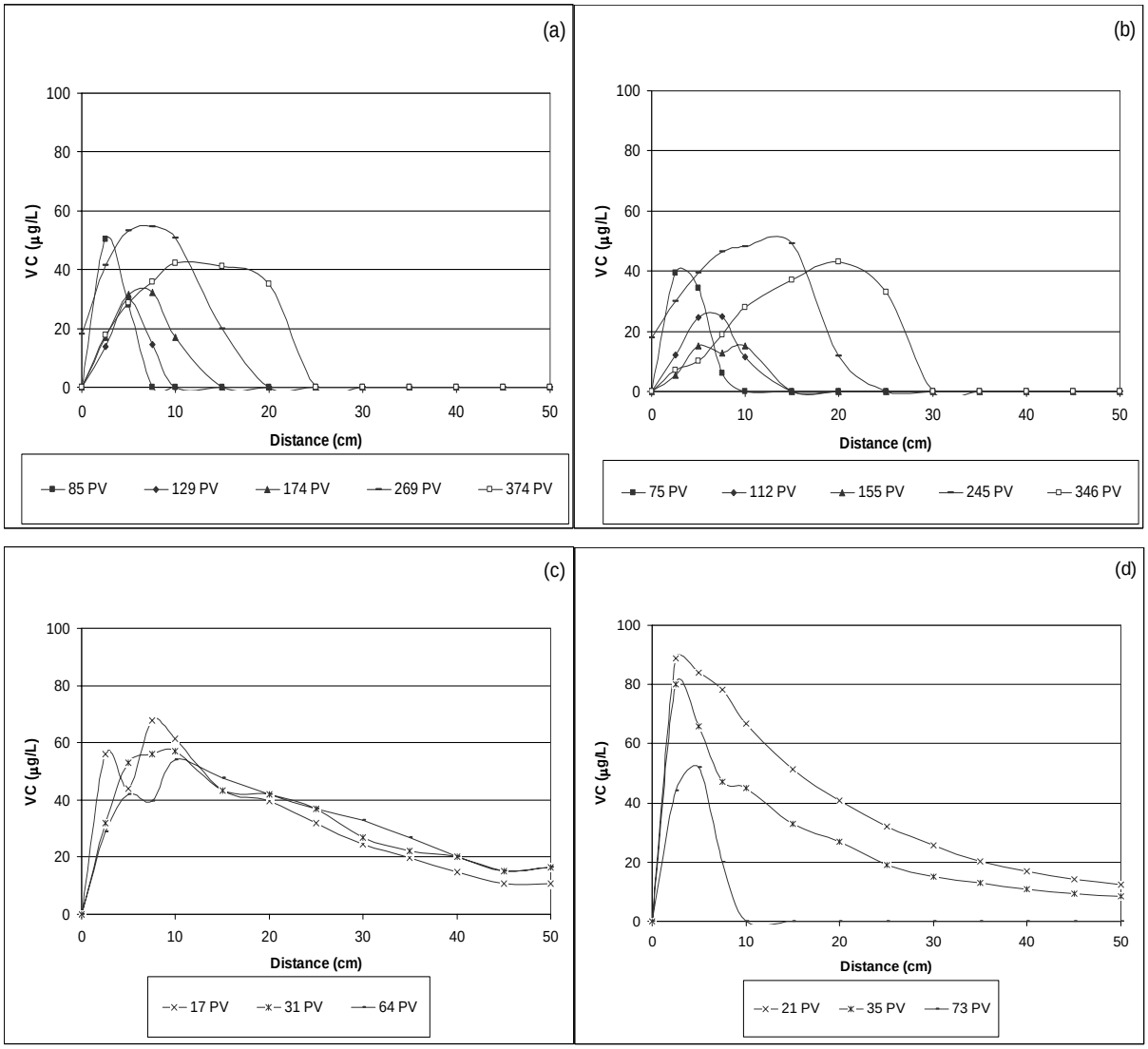

Fig. 3-3. The VC profiles for (a) Connelly, (b) G-M, (c) Ispat, and (d) Peerless iron. All PV represent pore volume after $CaCO_3$ addition.

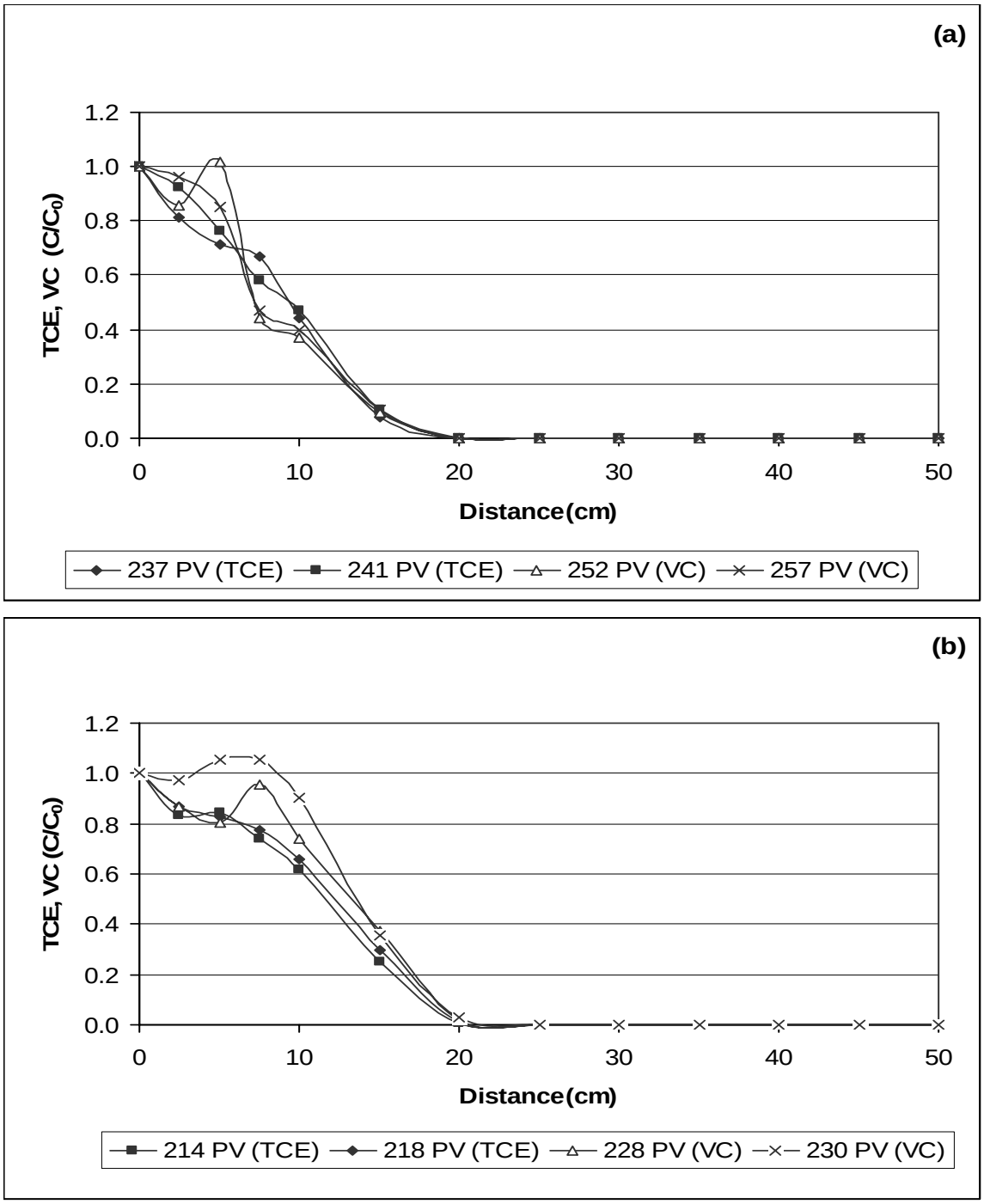

Fig. 3-4. The migration of the TCE and VC profiles for (a) Connelly and (b) G-M iron. All PV represent pore volume after $CaCO_3$ addition.

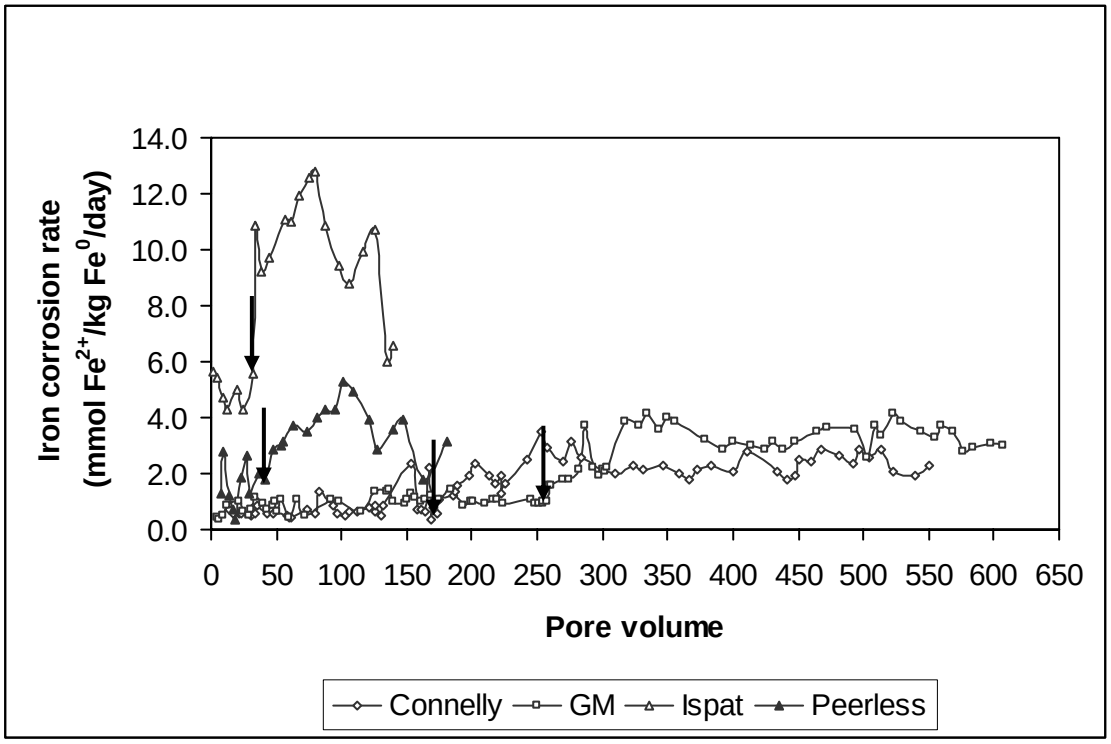

Fig. 3-5. Iron corrosion rate calculated from the rate of hydrogen evolution over time. Arrows indicate the time $CaCO_3$ was introduced to the column.

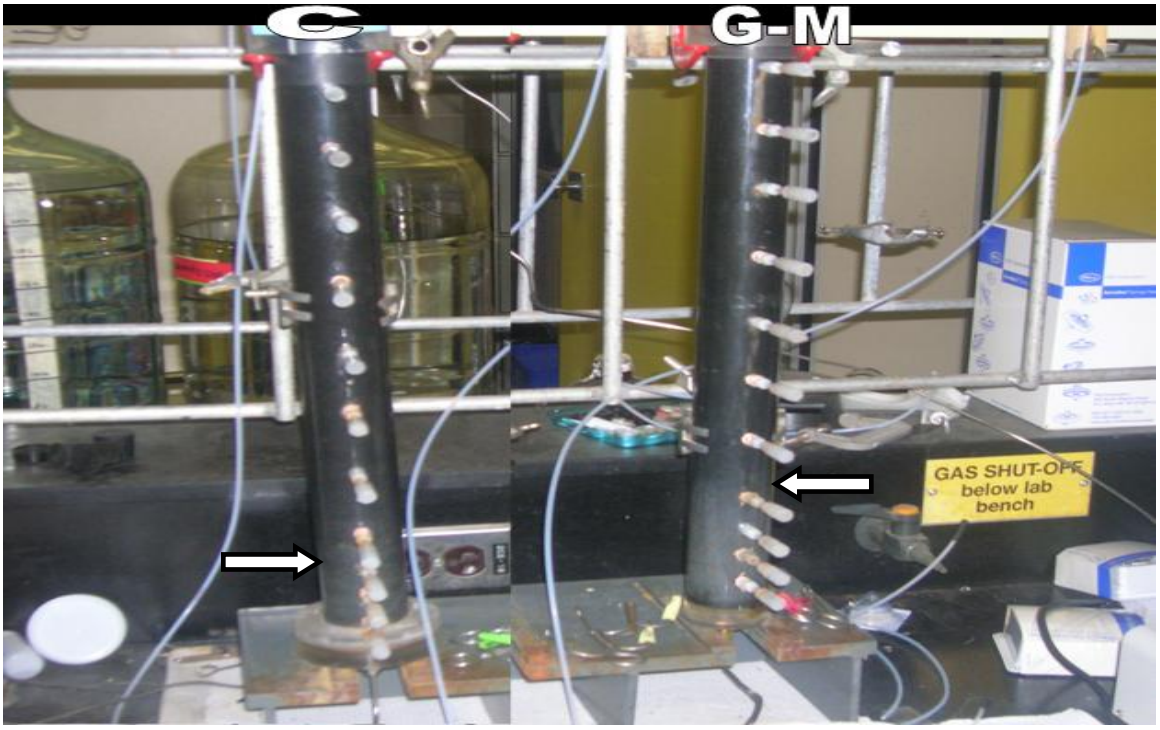

(a)

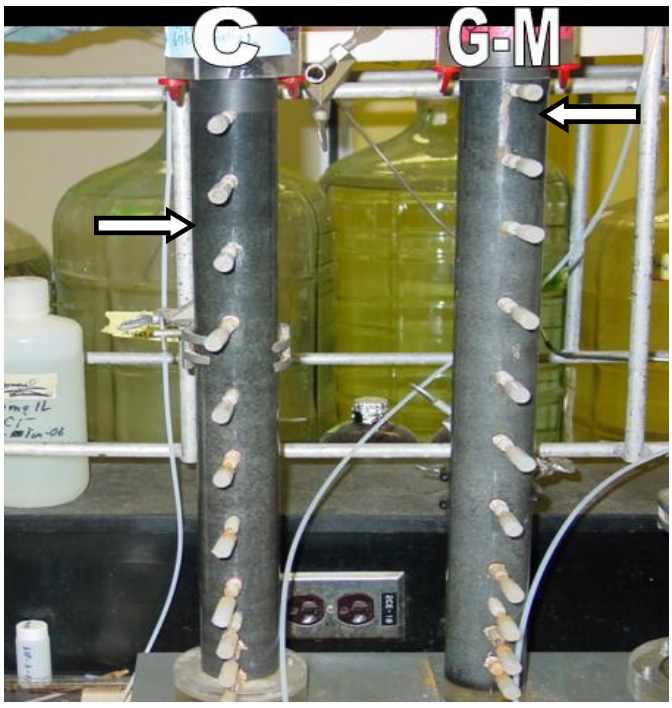

(b)

Fig. 3-6. The visual inspection after addition of $CaCO_3$ (a) for Connelly at 85 PV and for G-M at 77 PV and (b) for Connelly at 472 PV and for G-M at 435 PV. Arrows indicate the estimated precipitation fronts at selected pore volume.

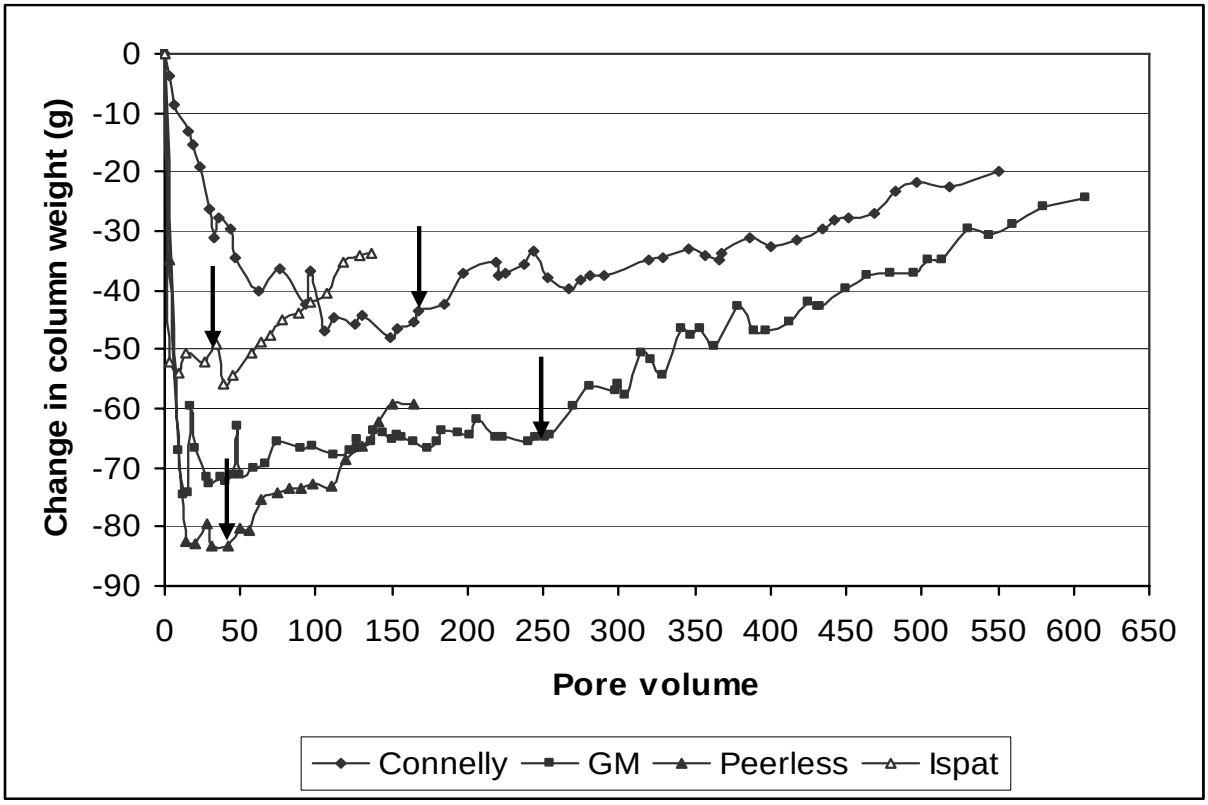

Fig. 3-7. Change in column weights measured over time for Connelly, G-M, Peerless and Ispat iron. Arrows indicate the time $CaCO_3$ was introduced to the column.

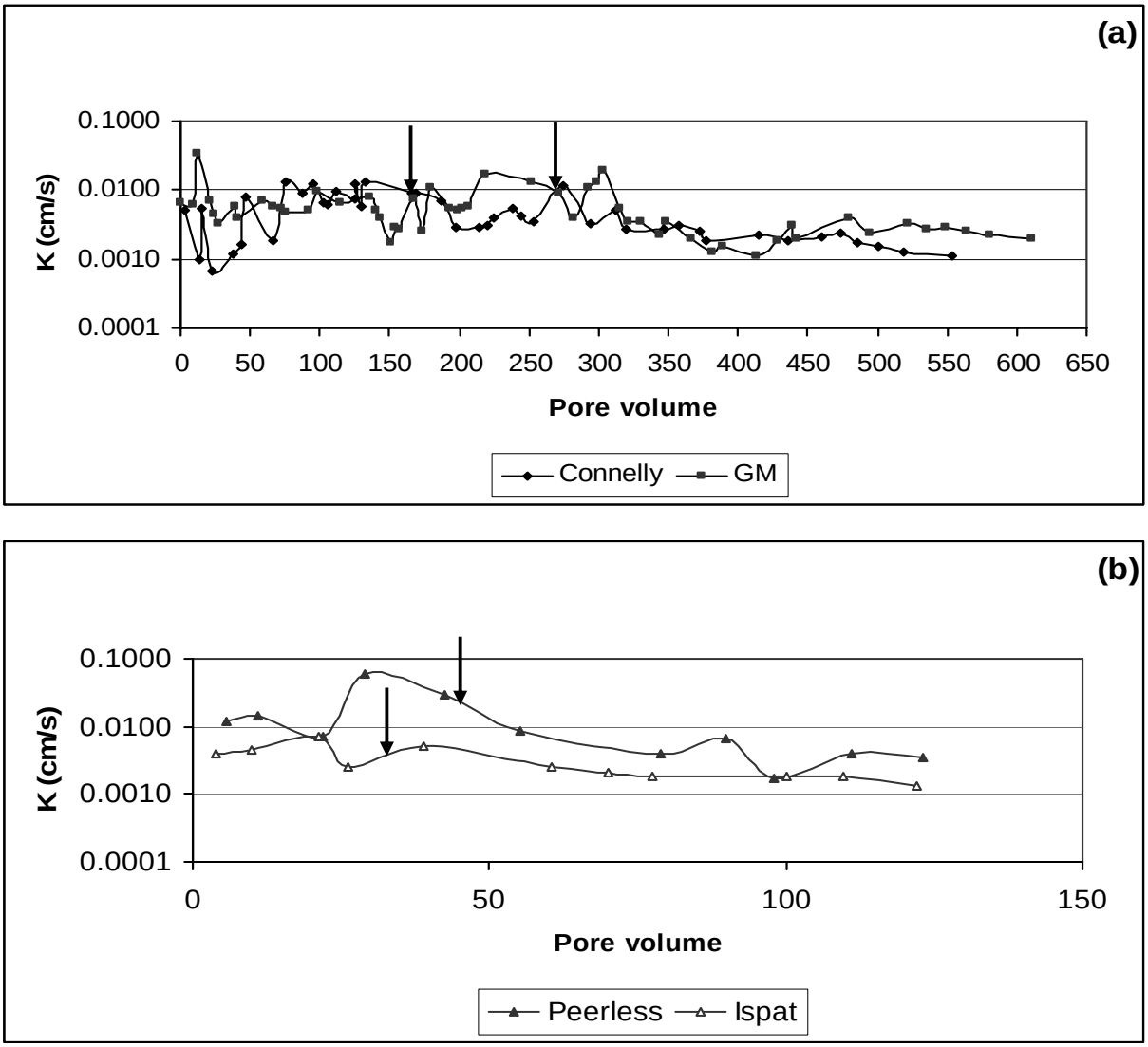

Fig. 3-8. The hydraulic conductivity (K) measured over time for (a) Connelly and G-M iron and for (b) Ispat and Peerless iron. Arrows indicate the time $CaCO_3$ was introduced to the column.

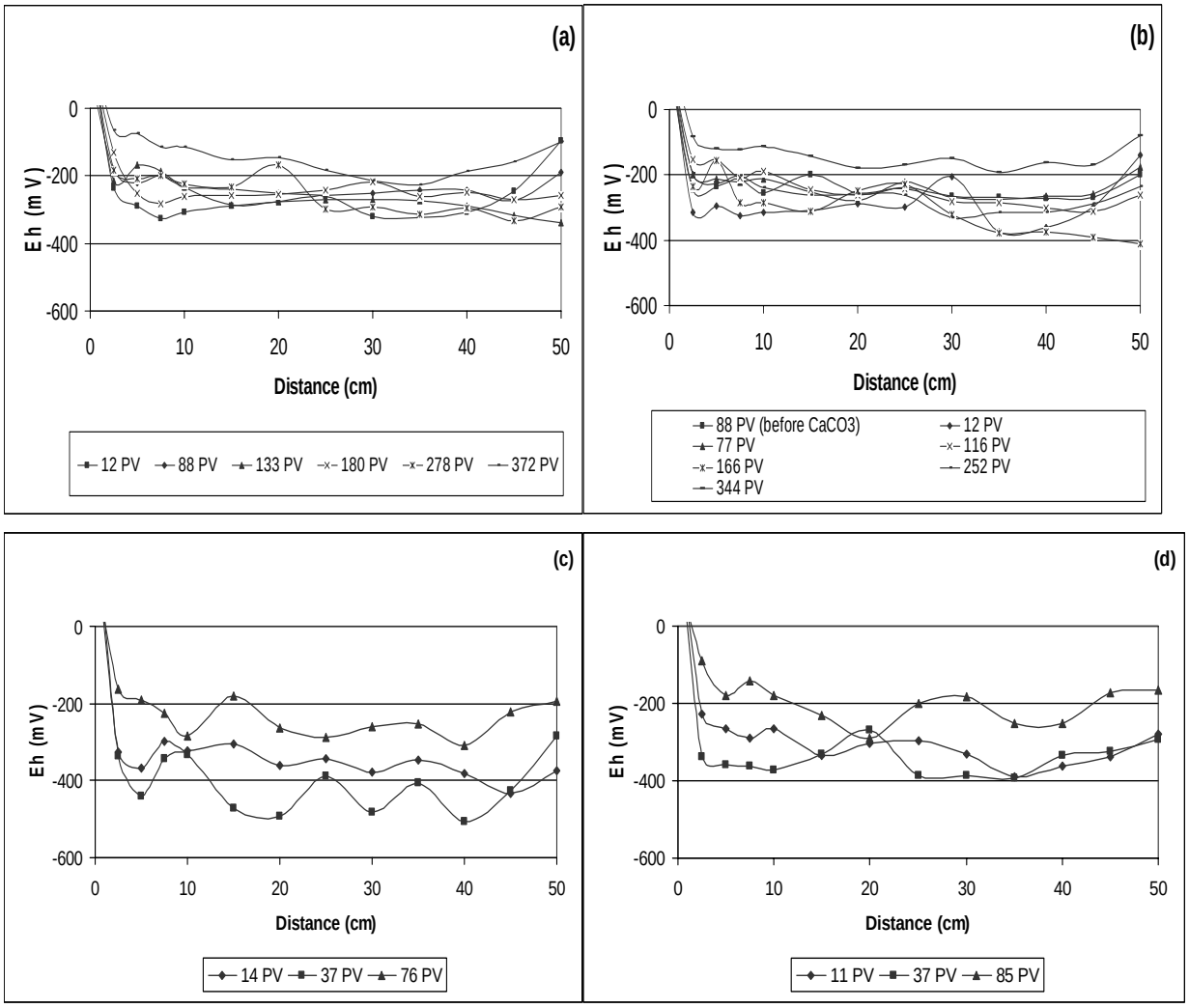

Fig. 3-9. The Eh profiles for (a) Connelly, (b) G-M, (c) Ispat and (d) Peerless iron. All PV represent pore volume after $CaCO_3$ addition, except for the first profile for G-M iron.

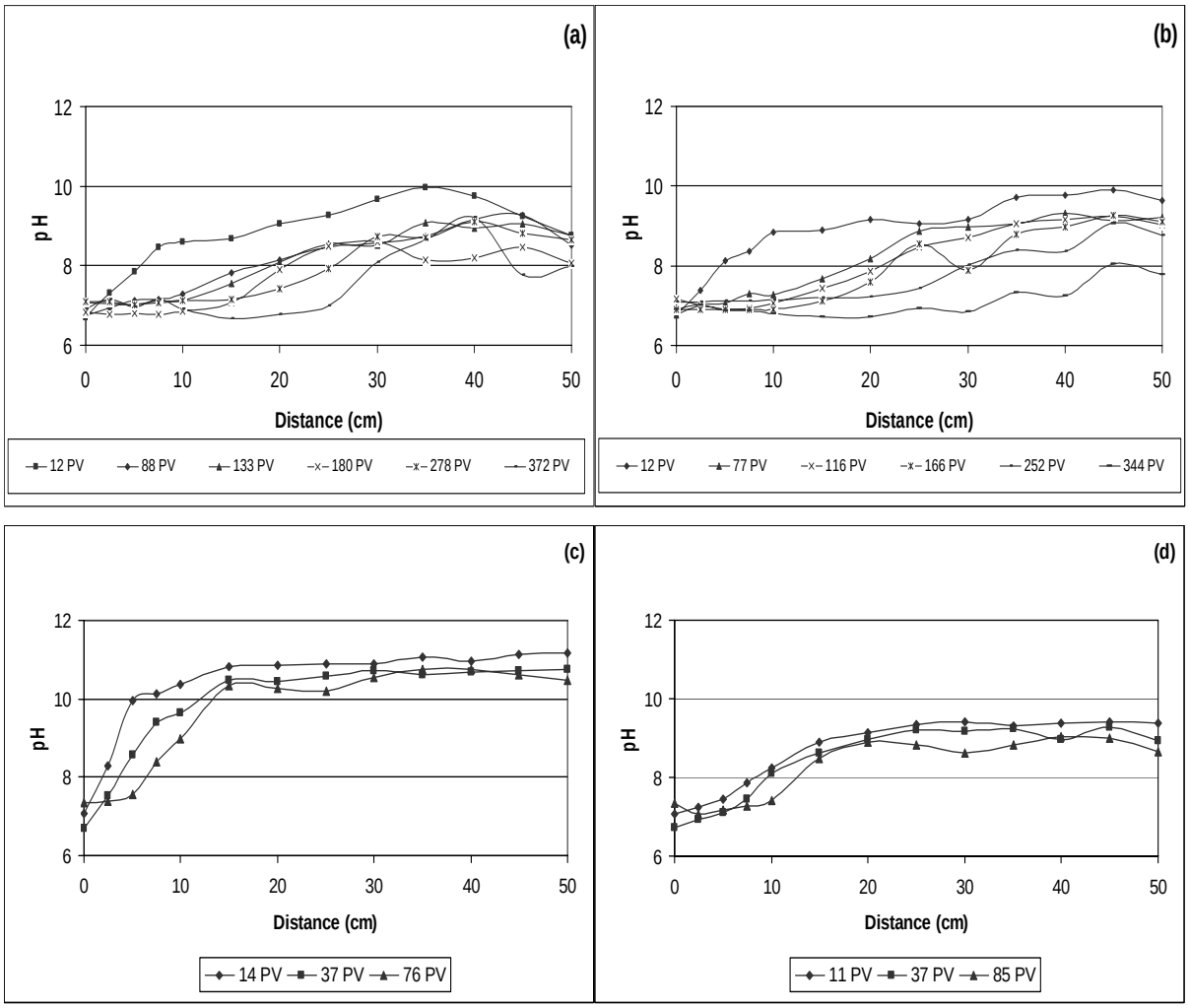

Fig. 3-10. The pH profiles for (a) Connelly, (b) G-M (c) Ispat and (d) Peerless iron. All PV represent pore volume after $CaCO_3$ addition.

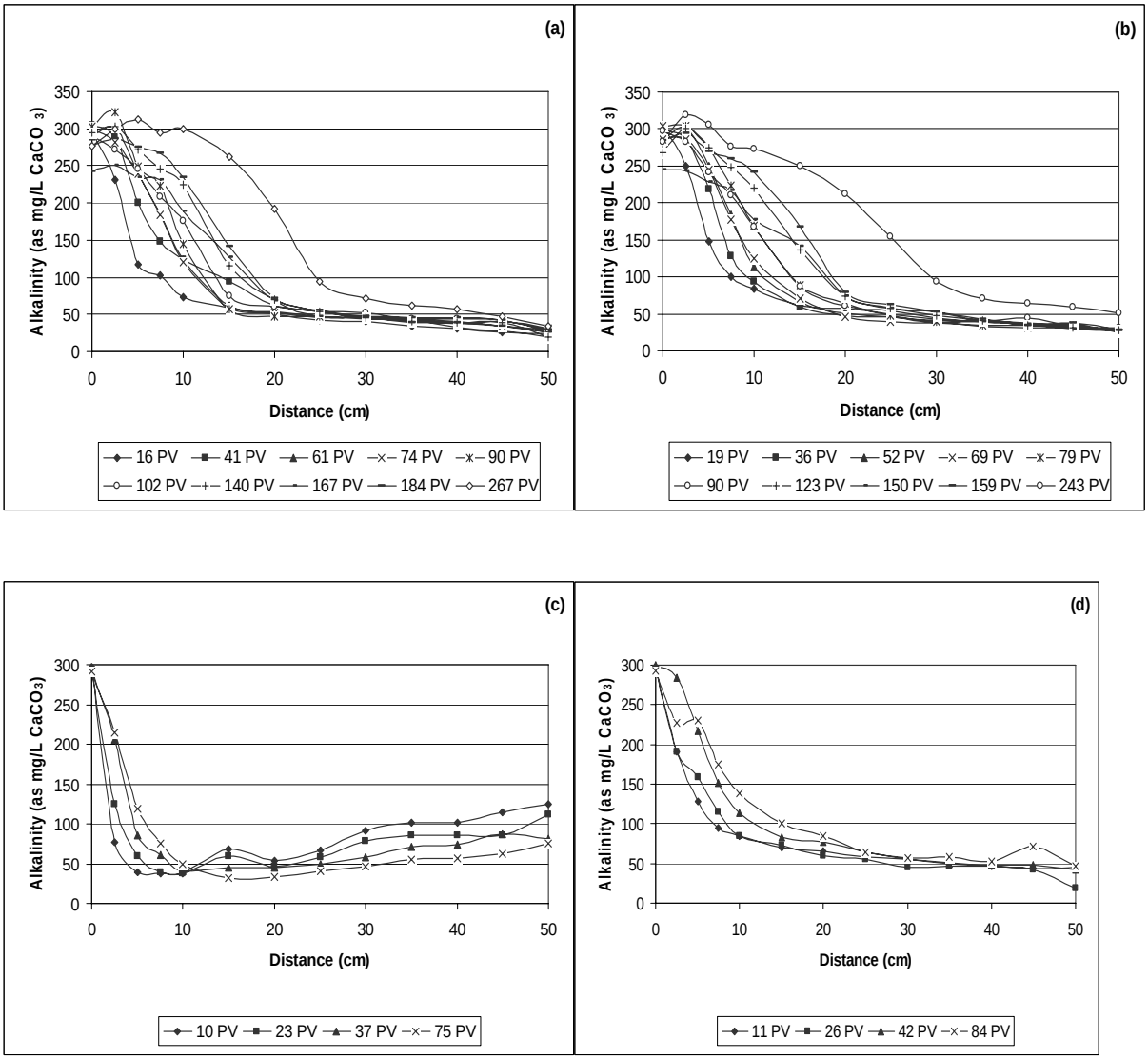

Fig. 3-11. The alkalinity profiles after $CaCO_3$ addition for (a) Connelly, (b) G-M, (c) Ispat and (d) Peerless iron. All PV represent pore volume after $CaCO_3$ addition.

4. Numerical Simulation

4-1. The reactive transport model (MIN3P) and modification

MIN3P (Mayer et al., 2002) includes various general kinetic formulations, including intra-aqueous and dissolution-precipitation reactions as well as geochemical equilibrium expressions for hydrolysis, aqueous complexation, oxidation-reduction, ion exchange, surface complexation, and gas dissolution-exsolution reactions. A more detailed description of the model can be found in Mayer et al. (2002).

The laboratory observations of Jeen (2005), as well as those reported in Zhang and Gillham (2005), showed that the reactivity of the iron decreased as precipitates accumulated. Jeen (2005) incorporated the decreasing reactivity of the iron into MIN3P by updating the surface area of the iron in the kinetic formulations, based on the proposed relationship between secondary mineral volume fraction and the surface area of the iron:

$$S(x,t) = S_0 \cdot \exp\left(-\sum a_i x_i(x,t)\right) \qquad (4\text{-}1)$$

where S(x,t) represents the surface area of the iron at a specific location along the flow path and time (m^2 iron L^- bulk), S_0 represents the initial surface area of the iron (m^2 iron L^- bulk), a_i is the proportionality constant for mineral phase i, which represents the extent to which that mineral phase contributes to the reactivity loss of the iron, and $x_i(x,t)$ is the volume fraction of the mineral phase i at a specific location and time (-). The surface area of the iron is the

mathematical representation of the reactivity of the iron at a certain time, and is used for convenience though it does not imply a particular mechanism of passivation.

In the model, the chemical reactions representative for the column systems, including cis-DCE degradation, iron corrosion, and secondary mineral precipitation, are considered. The rate for cis-DCE degradation is expressed as follows:

$$\frac{d[cis-DCE]}{dt} = -k_{SA-cis-DCE-Fe^0} \cdot S[cis-DCE] \tag{4-2}$$

where $k_{SA-cis-DCE-Fe^0}$ is the first-order rate constant for cis-DCE degradation normalized to the iron surface area (L H_2O m^{-2} iron s^{-1}) and $[cis-DCE]$ is the concentration of cis-DCE (mol L^{-1} H_2O). The iron corrosion rate is expressed in the form:

$$R_{H_2O-Fe^0} = -\max\left\{\left[k_{SA-H_2O-Fe^0} \cdot S\left(1-\frac{IAP_{H_2O-Fe^0}}{K_{H_2O-Fe^0}}\right)\right],0\right\} \tag{4-3}$$

where $k_{SA-H_2O-Fe^0}$ is the rate constant of iron corrosion normalized to the iron surface area (mol m^{-2} iron s^{-1}), *IAP* is the ion activity product, and *K* is the equilibrium constant. The rate expressions for secondary mineral precipitation are as follows:

$$R_i^m = \max\left\{\left[k_{eff,i}\left[1-\left(\frac{IAP_i^m}{K_i^m}\right)^{-1}\right]\right],0\right\} \tag{4-4}$$

where $k_{eff,i}$ is the effective rate constant for the precipitation of mineral phase *i* (mol L^{-1} H_2O s^{-1}), IAP_i^m is the ion activity product, and K_i^m is the corresponding equilibrium constant.

The surface area of iron in equations 4-2 and 4-3, representing the reactivity of the iron, decreases as mineral precipitation occurs. It is noted that the rate expressions for secondary mineral precipitation in equation 4-4 do not include the terms for the surface area of iron, but the rate change depending on the evolving geochemical conditions. Jeen (2005) modified the kinetic module in MIN3P by calculating the volume fractions of secondary minerals at each node at the end of each time step and updating the surface area of the iron at each node. Thus, the progressive migration of the contaminant removal profiles as well as geochemical changes over time were successfully simulated. In this study, the same modified code was applied to the results of the column experiments for Connelly and G-M iron to evaluate the applicability of the model and further estimate the longevity of iron PRBs containing iron materials with different reactivities. The simulation results were also used to test the initial hypothesis.

4-2. Model parameters

4-2-1. Chemical reactions

Based on the observed geochemical changes in the columns, the following 11 aqueous components were included for the expression of all chemical reactions: Ca^{2+}, Cl^-, CO_3^{2-}, Fe^{2+}, H^+, H_2(aq), TCE, cis-1,2-DCE, VC, ethene, and H_2O. A total of 12 aqueous complexes were also included for appropriate determination of mineral solubilities. The two reduction-

corrosion reactions considered for the simulations include cis-DCE degradation and iron corrosion, of which reaction stoichiometries are listed in Table 4-1.

The rate constants for cis-DCE degradation for each column were determined by fitting the earliest cis-DCE profile after $CaCO_3$ addition. Log $k_{SA-cis-DCE-Fe^0}$ values were -6.74 L H_2O m^{-2} iron s^{-1} and -6.65 L H_2O m^{-2} iron s^{-1} for Connelly and G-M iron, respectively (Table 4-2). The initial rates for iron corrosion by water for each column were calculated from the maximum hydrogen gas generation rates, using the method suggested by Reardon (1995, 2005). The values were then further adjusted to reproduce the best simulation fits. The corrosion rates used for the simulations were somewhat higher than the calculated values; however, the relative difference between the columns remained similar (Table 4-2).

Table 4-3 summarizes secondary mineral precipitation reactions considered for the simulations. Equilibrium constants for $CaCO_3$(s) (aragonite) and $Fe(OH)_2$(am) were from the databases of WATEQ4F (Ball and Nordstorm, 1991) and EQ3/6 (Wolery and Daveler, 1992), respectively. The equilibrium constant for $Fe_2(OH)_2CO_3$(s) was estimated from the aqueous concentrations by Jeen (2005).

4-2-2. Spatial discretization, physical parameters, and initial and boundary conditions

One-dimensional discretization was used to represent the column system. A spatial discretization interval of 0.01 m was used for the 0.5 m-long column, resulting in a total of 51 grid points. The initial porosities, calculated at the beginning of the experiments, were 0.46 for Connelly and 0.50 for G-M iron and the corresponding volume fractions of the granular iron were 0.54 for Connelly and 0.50 for G-M iron (Table 4-4). The initial hydraulic conductivities

determined for Connelly and G-M iron were 6.57×10^{-5} m/s and 7.10×10^{-5} m/s, respectively. A fully-saturated system with a second type (specified flux) boundary at the influent end and first type (specified head) boundary at the effluent end were used in the simulations. The flow rate of 5.89×10^{-6} m/s was used for the specified flux, and the hydraulic head at the effluent end was assigned a value of zero. The diffusion coefficient and longitudinal dispersivity were 1.5×10^{-9} m^2/s and 9.9×10^{-4} m, respectively. The measured aqueous concentrations and pH of the source solution were used for the influent chemical compositions. Table 4-4 summarizes the input parameters used in the simulations for each column.

4-2-3. Determining fitting parameters

The effective rate constants for the precipitation of $CaCO_3$(s) (aragonite) and $Fe_2(OH)_2CO_3$(s) were obtained by fitting the initial pH and alkalinity profiles simultaneously. The proportionality constants for aragonite and $Fe_2(OH)_2CO_3$(s) (i.e., a_1 and a_2 in Table 4-5) were determined by a trial-and-error method until the best fits for the entire profiles over time (i.e., the profiles of cis-DCE, alkalinity, pH, and carbonate volume fraction, etc.) were obtained. The effective rate constants for the precipitation of $CaCO_3$(s) (aragonite) and $Fe_2(OH)_2CO_3$(s) and the proportionality constants for each mineral phase are shown in Table 4-5.

4-3. Simulation results

4-3-1. Simulation results for the column experiments

The numerical simulations were intended to represent passivation of the iron materials caused by mineral precipitation after $CaCO_3$ addition. Thus, simulation results were only compared to the data after introduction of $CaCO_3$. Fig. 4-1 shows the measured and simulated profiles for cis-DCE over time for each column. The fitting parameters in Table 4-5 were compared to the parameters used in the simulations of Jeen (2005) and appeared to be comparable, except for the precipitation rate constant for $Fe_2(OH)_2CO_3(s)$ (Table 4-5) which were 1 ~ 2 orders of magnitude lower than determined by Jeen (2005). It is noted that Jeen (2005) used Connelly iron for the treatment of TCE at different concentrations of $CaCO_3$ (100 mg/L or 500 mg/L). The precipitation rate constant for aragonite was similar to those of Jeen (2005). The log k_{eff} values of -7.44 to -6.93 for aragonite and -10.89 to -9.75 for $Fe_2(OH)_2CO_3(s)$ were reported in Jeen (2005). The log k_{eff} value used in this study was -7.62 for aragonite and -11.74 for $Fe_2(OH_2)CO_3(s)$ (Table 4-5). The differences in geochemcial conditions may result in different precipitation rate constants for $Fe_2(OH)_2CO_3(s)$; however, another possible reason could also be the lack of constraints in this study. For the study of Jeen (2005), the calcium and dissolved iron concentrations were used as additional constraints for determining the precipitation rates for $Fe_2(OH)_2CO_3(s)$; however, no such data was available for this study. The proportionality constants for each mineral phase determine the extent to which reactivity of the iron is decreased due to the accumulation of that particular mineral phase. The proportionality constant for aragonite in this study was 95.0, compared to the range

of 55.0 ~ 85.0 from Jeen (2005). The proportionality constant for $Fe_2(OH)_2CO_3(s)$ was 0 for this study and 2.0 ~ 5.0 for Jeen (2005), implying a substantially geater effect of aragonite than $Fe_2(OH)_2CO_3(s)$ on the reactivity loss of the iron in both studies.

It is important to note that except for the iron corrosion rates (Table 4-2), indicative of reactivities of the irons, all other fitting parameters are the same for both columns (Table 4-5). Thus, the differences in the simulated performance of the two columns were due solely to the difference in iron corrosion rates. This indicates that matching the data was not simply a random curve fitting process. It would appear that changing the reactivity resulted in changes in profile behaviour that were consistent with the data. This also suggests that if the reactivity of the iron material can be represented by the iron corrosion rate, the performance of different iron materials in similar geochemical conditions may be predicted.

The simulated cis-DCE profiles were not precisely matched with the individually-measured profiles (Fig. 4-1). For example, the curvatures in the region close to the influent end were not reproduced completely. Nevertheless, the simulated profiles for both columns gave good representation of the major trends in the data. More importantly, the significant difference in the pattern of passivation was successfully demonstrated. For example, consistent with the laboratory observations, for Connelly, there was no expanding (highly passivating) zone where there appeared to be little degradation. On the other hand, the expanding zone adjacent to the influent end for G-M, resulting from the higher iron corrosion rate (Table 4-2), was reflected in the simulation results. Furthermore, the simulations showed the leading edge of the degradation profiles to be somewhat advanced in G-M relatively to Connelly.

The matching of the alkalinity profiles between the measured and simulated results was also relatively successful (Fig. 4-2). It should be noted that the simulation periods for cis-DCE

(170 days for both columns, Fig. 4-1) and alkalinity (122 days for Connelly and 121 days for G-M, Fig. 4-2) are different. The first simulated alkalinity profile for G-M was slightly steeper than for Connelly (Fig. 4-2), indicating a higher removal rate at early time consistent with the laboratory results. Thus, the progression of the passivation front should have caused a faster migration of the alkalinity profile for G-M. However, a faster consumption of alkalinity in the still relatively reactive regions, due to higher corrosion rate, may have compensated somewhat for the passivation. Thus, the differences in migration of the alkalinity profiles between the two columns was less obvious than for cis-DCE. Over time, the simulated alkalinity profiles over time were very similar for the two columns consistent with measurement. At the time of the last alkalinity samplings, there was no major difference between the results for the two columns (Fig. 3-11 (a) and (b)).

Fig. 4-3 shows the simulated aragonite volume fractions for Connelly and G-M iron. At early times, aragonite accumulated in the region close to the influent end. As passivation proceeded, the precipitation front proceeded further into the column in both cases. Compared to Connelly, G-M iron showed slightly more aragonite accumulation near the influent end, indicating more passivation in that region. Fig. 4-4 shows the simulated porosity for Connelly and G-M iron. The loss in porosity in the region near the influent end was greater in G-M iron than in Connelly due to greater accumulation of precipitates in that region. Connelly iron, on the other hand, showed a slightly greater spread in porosity loss along the column.

The model provided a reasonable representation of the effects of changing reactivity; however, the results are not entirely conclusive because of the relatively small differences in reactivity between the iron materials and thus relatively small differences in the behaviour of

the various profiles. Nevertheless, the results support the use of the model as a tool for predicting long-term performance of PRBs using iron materials of differing reactivity.

4-3-2. Long-term prediction

Further simulations were performed to predict the differences in performance over longer periods of time for different iron materials with differing initial reactivities. The performance of a 50 cm-thick iron PRB, treating 10 mg/L cis-DCE, with a groundwater composition of 300 mg/L $CaCO_3$ and a velocity of 10 cm/day, over a period of 40 years was simulated. For the four cases tested, the characteristics of the iron materials, such as iron corrosion rates and initial cis-DCE degradation rates, were selected from the values representative of Connelly, G-M, Ispat and Peerless, as measured in this study. The maximum values of the measured iron corrosion rates for the four irons were used as representative values of the initial iron corrosion rate. The initial iron corrosion rates used in the simulations were Log $k_{SA-H_2O-Fe^0}$ = -10.53, -10.00, -9.95 and -9.61 for Connelly, G-M, Peerless, and Ispat, respectively, showing that Ispat has the highest rate followed by Peerless, G-M and Connelly. The cis-DCE degradation constants used were from Table 3-1, with Log $k_{SA-cis-DCE-Fe^0}$ = - 6.74, - 6.65, - 7.04, and - 7.60 for Connelly, G-M, Peerless, and Ispat, respectively. The pH of the inflowing water was assumed to be 6.9 and the porosity and hydraulic conductivity of the PRB was assumed to be 0.5 and 6.57 x 10^{-5} m/s, respectively. All other parameters were brought from the values of Tables. 4-4 and 4-5, used in the previous simulations for Connelly and G-M.

Fig. 4-5 shows the predicted breakthrough curves for cis-DCE at the effluent face of the PRB for the four iron materials. Under the imposed conditions, cis-DCE began to breakthrough

the PRB after about 9, 12, 13 and 15 years of operation, for Ispat, Peerless, G-M and Connelly, respectively. Ispat, which has the highest corrosion rate (Fig. 3-5) and the lowest cis-DCE degradation rate (Table 3-1), showed the earliest breakthrough, representing the worst performance. On the other hand, Connelly, which has the lowest corrosion rate (Fig. 3-5) and the highest cis-DCE degradation rate (Table 3-1), showed the latest breakthrough. The steepness of the breakthrough curves was also dependent on the corrosion rate; i.e, the materials with higher corrosion rates had steeper curves than those of lower rates. Depending upon the initial concentration and the MCL, this could have important consequences. For example, if the MCL corresponds to a C/C_0 value of 0.2, the Connelly iron would perform adequately for a period of about 23 yr, while Ispat would fail at about 13 yr.

The predictions for the porosity reduction are shown in Fig. 4-6 for a ten-year (a) and 40-year (b) simulation**.** The cases with higher corrosion rates showed greater reduction in porosity near the influent end at early times (Fig. 4-6 (a)) because of greater accumulation of carbonate minerals in that region. Over time, the reduction in porosity was spread further into the barrier for all cases, and was simply dependent on the initial corrosion rates (Fig. 4-6 (b)), indicating that the cases of lower corrosion rates have better performance in terms of permeability.

In summary, the predictions support the hypothesis that iron material having lower initial corrosion rate would be more beneficial than iron having higher corrosion rates for long-term operation of PRBs. The accurate determination of model parameters, such as initial cis-DCE degradation rate constants and iron corrosion rates, are required for better predictions of long-term performance.

Table 4-1. Reaction stoichiometries of reduction-corrosion reactions.

cis-DCE degradation	$Fe^0(s) + C_2H_2Cl_2 + H^+ \rightarrow Fe^{2+} + C_2H_3Cl + Cl^-$
Iron corrosion	$Fe^0(s) + 2H_2O \rightarrow Fe^{2+} + H_2(aq) + 2OH^-$

Table 4-2. Reaction rate constants and the initial surface area of the iron.

Parameter	Column	
	Connelly	G-M iron
$\log k_{SA-cis-DCE-Fe^0}$ (L H_2O m^{-2} iron s^{-1})	-6.74	-6.65
Initial reactive surface area[a] (m^2 iron L^{-1} bulk)	4.48×10^3	1.80×10^3
$\log k_{SA-H_2O-Fe^0}$ [b] (mol m^{-2} iron s^{-1})	-9.92 (-10.53)	- 9.38 (-10.00)

[a]Measured using BET (Brunauer et al., 1938) analyses.

[b]Initiated from the measured gas generation rates, and was further adjusted to reproduce the best simulation results. The values in parentheses represent the maximum corrosion rate calculated from the measured rates of gas generation.

Table 4-3. Mineral dissolution-precipitation reactions and equilibrium constants.

Reaction	log K
$CaCO_3(s)(aragonite) \Leftrightarrow Ca^{2+} + CO_3^{2-}$	8.360[a]
$Fe_2(OH)_2CO_3(s) \Leftrightarrow 2Fe^{2+} + CO_3^{2-} + 2H_2O - 2H^+$	0.075[b]
$Fe(OH)_2(am) \Leftrightarrow Fe^{2+} + 2H_2O - 2H^+$	–13.905[c]

[a]From WATEQ4F database (Ball and Nordstrom, 1991).

[b]Estimated from the aqueous concentrations (Jeen, 2005).

[c]From EQ3/6 database (Wolery and Daveler, 1992).

Table 4-4. Input parameters used in the simulations.

Parameter	Column	
	Connelly	G-M
Column length (m)	0.50	
Fe^0 volume fraction (-)	0.54	0.50
Porosity (-)	0.46	0.50
Hydraulic conductivity (m/s)	6.57×10^{-5}	7.10×10^{-5}
Diffusion coefficient[a] (m^2/s)	1.5×10^{-9}	
Longitudinal dispersivity[b] (m)	9.9×10^{-4}	
Running time (Days)	170	
Flow rate (m/s)	5.89×10^{-6}	
pH	7.08	
Ca^{2+} (mol/L)	3.0×10^{-3}	
Total C (mol/L)	7.50×10^{-3}	
cis-DCE (mol/L)	1.03×10^{-4}	

[a]From Freeze and Cherry (1979).

[b]From a bromide tracer test (Jeen, 2005).

Table 4-5. Fitting parameters for each column.

Parameter		Connelly	G-M	Jeen (2005)
log k_{eff} (mol L^{-1} H_2O s^{-1})	$CaCO_3$(s) (aragonite)	-7.62		-7.44 ~ -6.93
	$Fe_2(OH)_2CO_3$(s)	-11.74		-10.89 ~ -9.75
a_1[a]		95.0		55.0 ~ 85.0
a_2[b]		0		2.0 ~ 5.0

[a]Proportionality constant for $CaCO_3$(s) (aragonite).

[b]Proportionality constant for $Fe_2(OH)_2CO_3$(s).

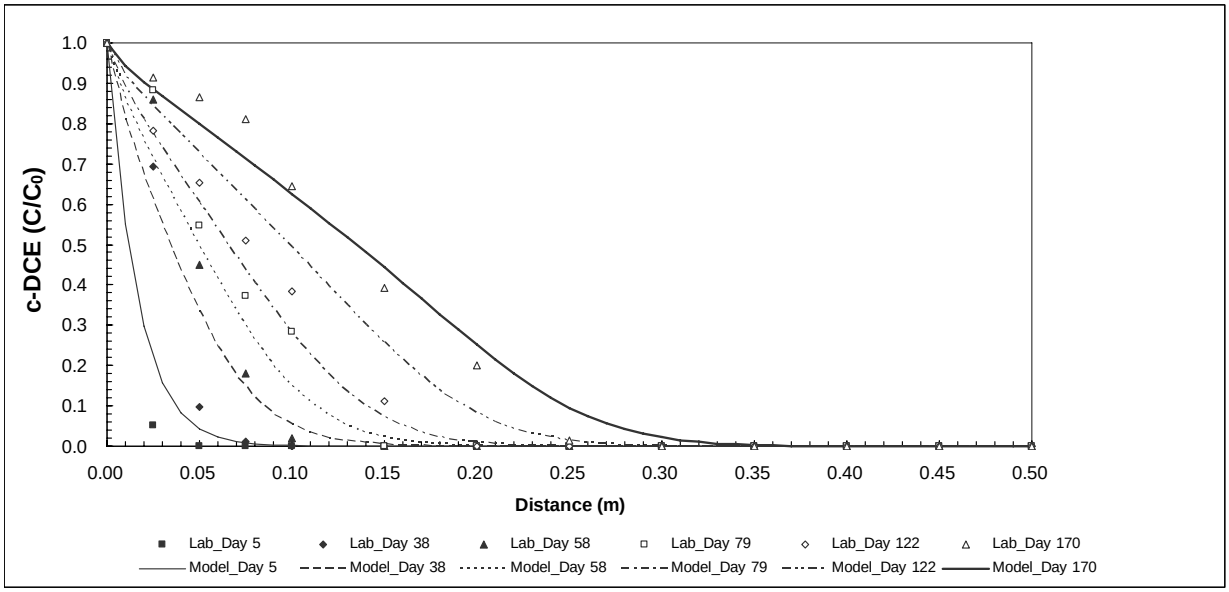

(a)

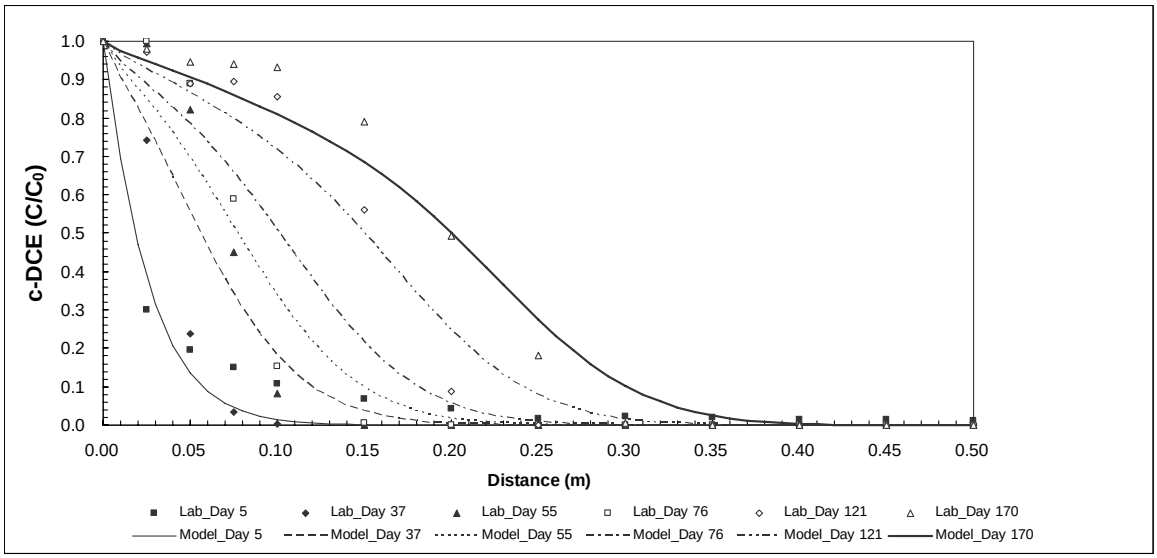

(b)

Fig. 4-1. Measured and simulated profiles for cis-DCE: (a) Connelly and (b) G-M iron.

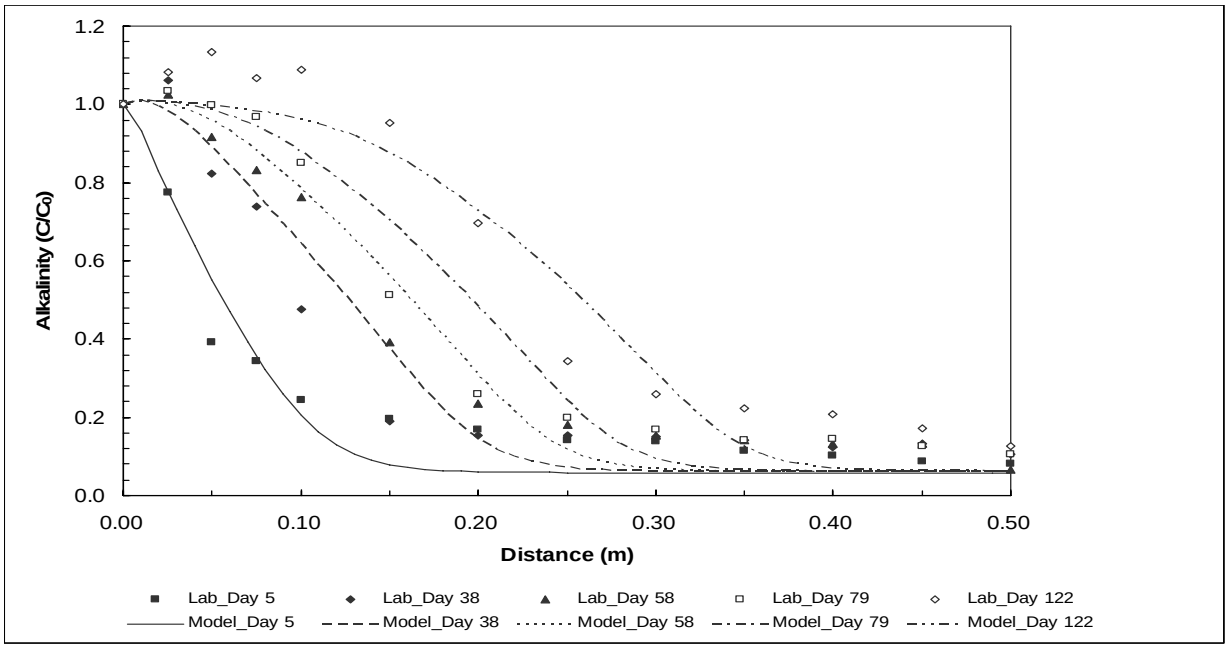

(a)

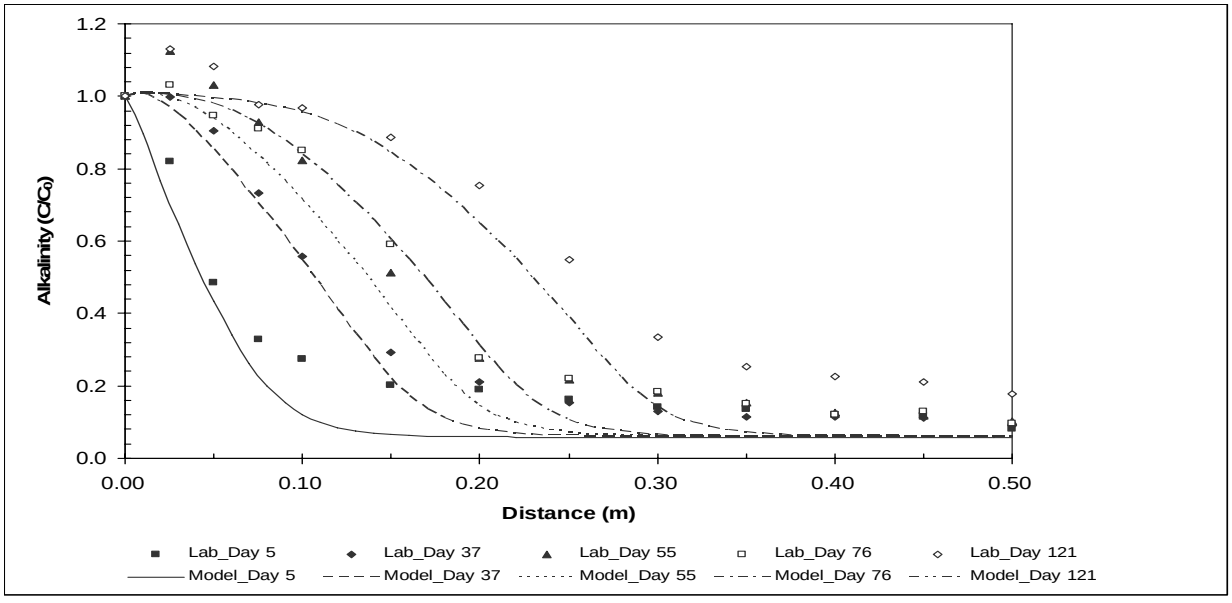

(b)

Fig. 4-2. Measured and simulated profiles for alkalinity: (a) Connelly and (b) G-M iron.

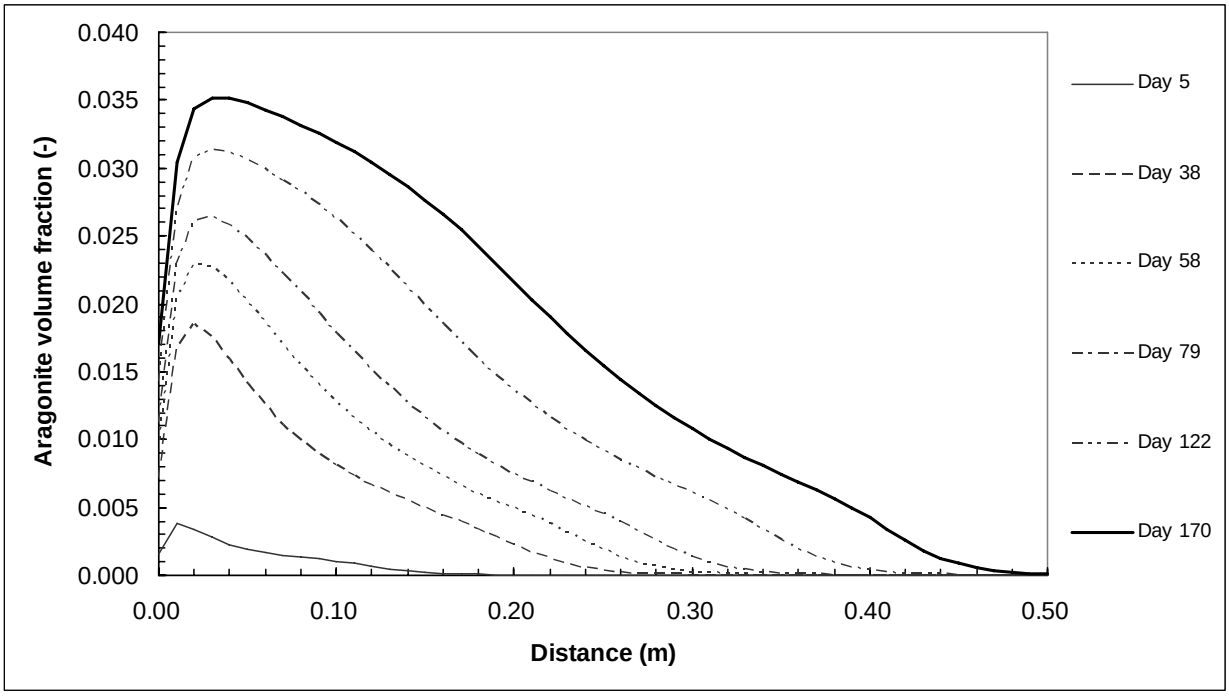

(a)

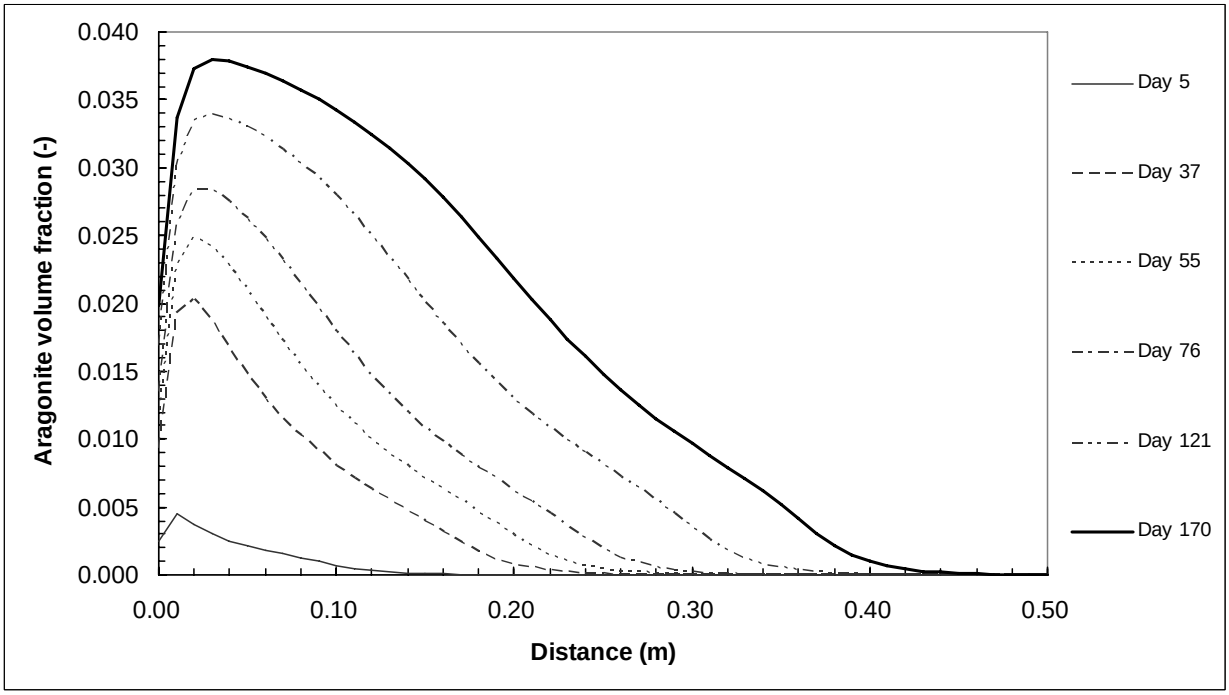

(b)

Fig. 4-3. Simulated aragonite volume fraction for (a) Connelly and (b) G-M iron.

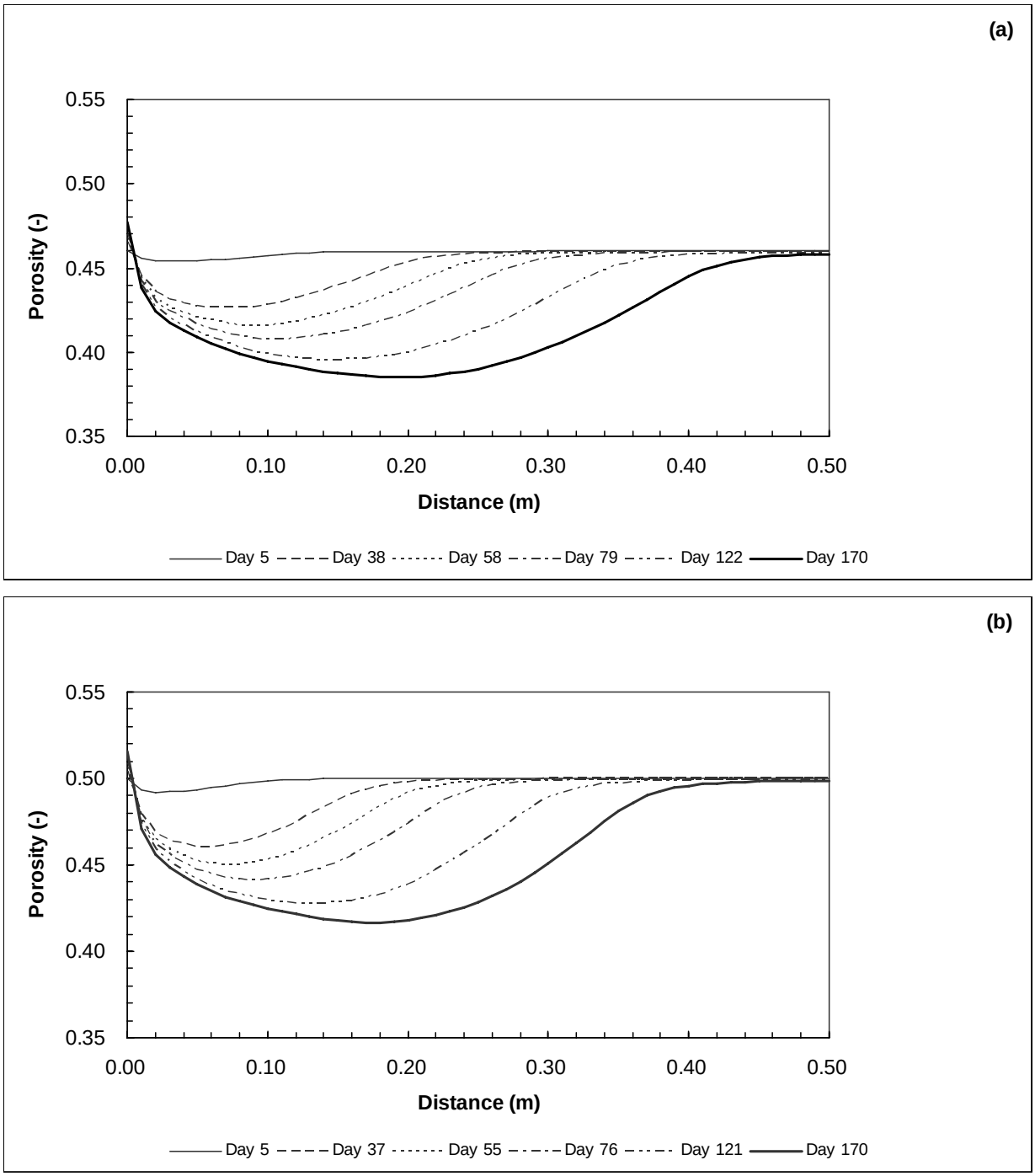

Fig. 4-4. Simulated porosity for (a) Connelly and (b) G-M iron.

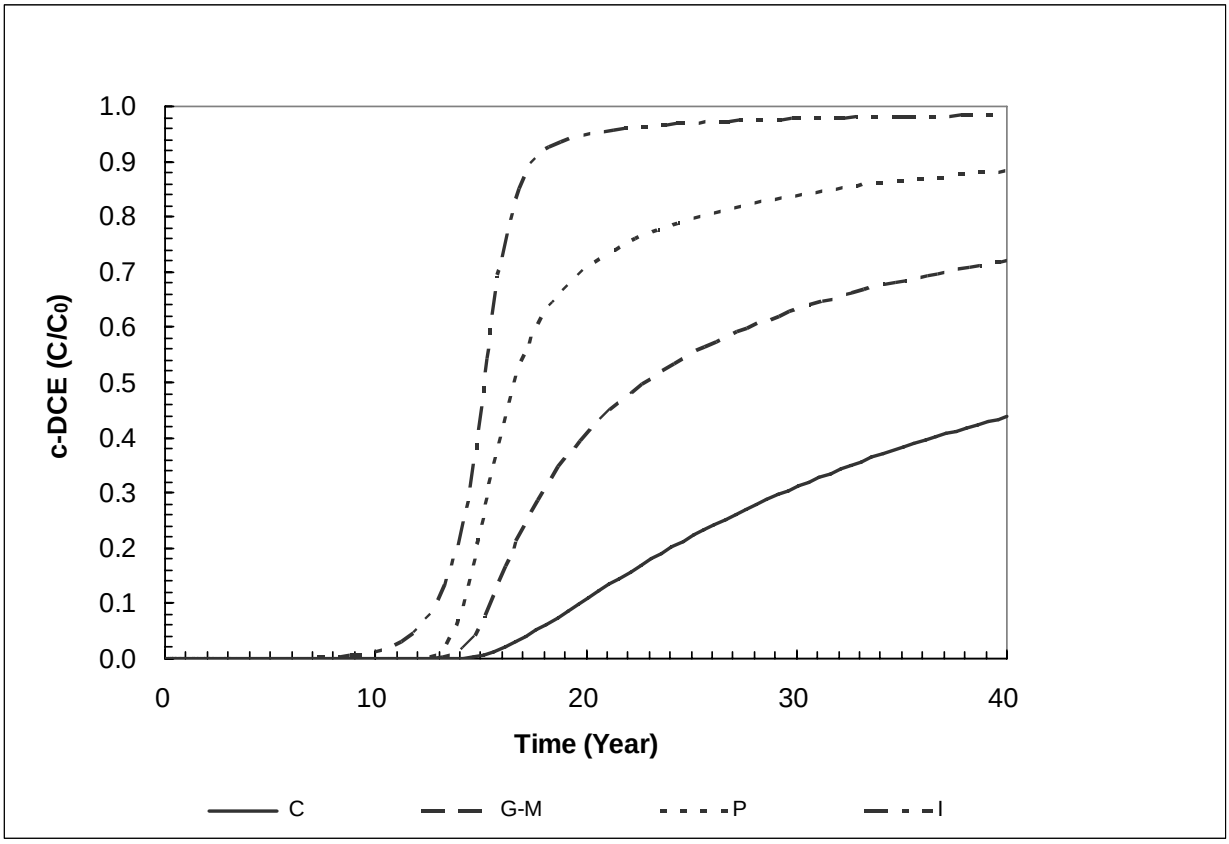

Fig. 4-5. Predicted breakthrough curves at the effluent end of the PRB for four different irons (C: Connelly, G-M: Gotthart-Maier, P: Peerless, I: Ispat). The simulations were performed using the iron corrosion rates, the iron surface areas and cis-DCE rate constants, obtained from the lab experiments.

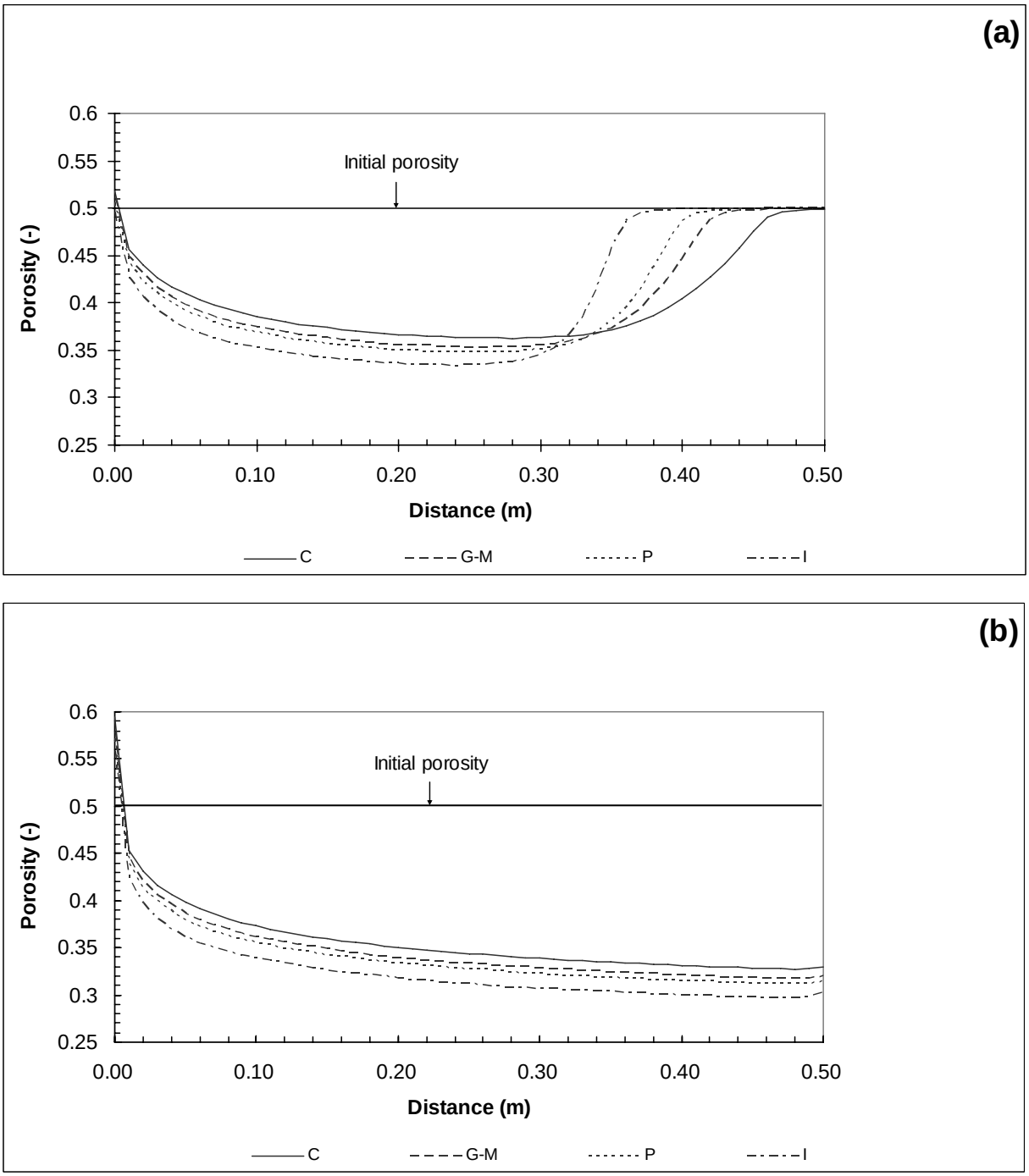

Fig. 4-6. Predicted porosity loss along the length of the PRB for four different irons (C: Connelly, G-M: Gotthart-Maier, P: Peerless, I: Ispat) after (a) 10 years and (b) 40 years.

5. Conclusions

A previous modeling study suggested that iron material having moderate reactivity may be more beneficial than material having a higher reactivity in terms of long-term performance because of less overall accumulation of secondary precipitates. The objective of this study was to evaluate the validity of the hypothesis and the changes of the reactivities of different iron materials in the presence of dissolved $CaCO_3$. The changes in iron reactivity over time in the presence of dissolved $CaCO_3$ were evaluated using four different iron sources with different initial reactivities (Connelly, G-M, Ispat and Peerless). The column experimental results showed that the accumulation of carbonate precipitates caused the passivation for all the columns. The passivation of the iron resulted in the migration of cis-DCE, TCE, VC and mineral precipitation fronts as well as other profiles including alkalinity, Eh, pH, and chloride.

The results for Connelly and G-M iron, which had organic and inorganic data for longer periods of time, were primarily evaluated to test the hypothesis. G-M iron had the higher initial corrosion rate compared to Connelly iron and thus had potential for faster accumulation of precipitates. The precipitation front migrated further and the slope of the increase in column weight was somewhat steeper for G-M iron. The total amounts of precipitates accumulated per pore volume was slightly more for G-M iron than for Connelly. Thus, the results appeared to support faster accumulation of precipitates for G-M. These differences in the accumulated precipitates resulted in a difference in the leading edge of organic profiles and a significant difference in the pattern of passivation. The leading edge of the cis-DCE profiles for G-M iron was somewhat further advanced than in the case of Connelly. While G-M iron showed a highly passivated zone adjacent to the influent end, passivation of Connelly appeared more as a

decline in slope of the degradation profile, starting from the influent end, with minor evidence of a highly passivated zone. Also, the profiles of TCE and VC, supplied as alternate contaminants in the source solution, showed a similar passivation shape, indicating greater passivation in the region near the influent end for G-M. Thus, the hypothesis appeared to be supported by experimental data, although the differences in the performance between the two columns were not great.

Model simulations were performed to further test the hypothesis. All fitting parameters for Connelly and G-M iron were the same, except for the initial corrosion rates. The iron corrosion rate was used as an indicator for the iron reactivity, and was one of the important model parameters for the application of the model (Jeen, 2005). The behaviour for the simulated organic and inorganic profiles were consistent with the experimental data, and differences in performance between the two columns were demonstrated solely by the differences in iron corrosion rates, supporting the hypothesis.

The simulations for long-term performance were conducted to predict the difference in performance over time for different iron materials with differing initial reactivities. The cases of higher corrosion rates showed earlier breakthroughs and steeper curves than those of lower corrosion rates. The relative steepness of the curves and breakthrough time was dependent on the iron corrosion rates. The predictions also showed that the cases of higher iron corrosion rates had more reduction in porosity near the influent surface at early times, due to more accumulation of carbonate minerals in that region. Over time, the reduction in porosity was spread further into the barrier, showing greater porosity loss for higher corrosion rate. Thus, long-term predictions support the hypothesis that iron material having moderate initial corrosion rate would be more beneficial than iron having higher corrosion rates for long-term

operation of PRBs. Accurate determination of model parameters such as iron corrosion rates and cis-DCE degradation rate constants are required for better predictions of long-term performance.

References

Agrawal, A., W.J. Ferguson, B.O. Gardner, J.A. Christ, J.Z. Bandstra, and P.G. Tratnyek. 2002. Effects of Carbonate Species on the Kinetics of Dechlorination of 1,1,1-Trichloroethane by Zero-Valent Iron. *Environmental Science and Technology*, 36 (20), 4326-4333.

Agrawal, A., and P.G. Tratnyek. 1996. Reduction of Nitro Aromatic Compounds by Zero-Valent Iron Metal. *Environmental Science and Technology*, 30 (1), 153-160.

Ball, J.W., and D.K. Nordstrom. 1991. *User's Manual for WATEQ4F, with Revised Thermodynamic Database and Test Cases for Calculating Speciation of Major, Trace and Redox Elements in Natural Waters*. U.S. Geological Survey, Open-File Report 91-183, 189 pp.

Blowes, D.W., and K.U. Mayer. 1999. An *In-Situ* Permeable Reactive Barrier for the Treatment of Hexavalent Chromium and Trichloroethylene in Ground Water: Volume 3, Multicomponent Reactive Transport Modeling. EPA/600/R-99/095c, U.S. Environmental Protection Agency, Washington, DC, September 1999.

Blowes, D.W., C.J. Ptacek, S.G. Benner, C.W.T. McRae, T.A. Bennett, and R.W. Puls. 2000. Treatment of Inorganic Contaminants Using Permeable Reactive Barriers. *Journal of Contaminant Hydrology*, 45, 123-137.

Brunauer, S., P.H. Emmett, and E. Teller. 1938. Adsorption of Gases in Multimolecular Layers. *Journal of American Chemical Society*, 60, 309-319.

Dean, J.A. 1992. *Lange's Handbook of Chemistry*. 14th ed., McGraw-Hill Inc., New York.

Devlin, J.F., J. Klausen, and R.P. Schwarzenbach. 1998. Kinetics of Nitroaromatic Reduction on Granular Iron in Recirculating Batch Experiments. *Environmental Science and Technology*, 32 (13), 1941-1947.

EnviroMetal Technologies Inc. (ETI), http://www.eti.ca (accessed June 2006).

Freeze, R.A., and J.A. Cherry. 1979. *Groundwater*. Prentice-Hall Inc., Englewood Cliffs, NJ, 604 pp.

Gillham, R.W., and S.F. O'Hannesin. 1994. Enhanced Degradation of Halogenated Aliphatics by Zero-Valent Iron. *Ground Water*, 32 (6), 958-967.

Gu, B., T.J. Phelps, L. Liang, M.J. Dickey, Y. Roh, B.L. Kinsall, A.V. Palumbo, and G.K. Jacobs. 1999. Biogeochemical Dynamics in Zero-Valent Iron Columns: Implications for Permeable Reactive Barriers. *Environmental Science and Technology*, 33 (13), 2170-2177.

Gui, J., and T.M. Devine. 1995. A SERS Investigation of the Passive Films Formed on Iron in Mildly Alkaline Solutions of Carbonate/Bicarbonate and Nitrate. *Corrosion Science*, 37 (8), 1177-1189.

Jeen, S., 2005. Effects of Mineral Precipitation on Long-Term Performance of Granular Iron Permeable Reactive Barriers: Column Experiments and Numerical Simulation. Ph. D. Thesis, Department of Earth Sciences, University of Waterloo, Ontario, Canada, 237 pp.

Johnson, T.L., M.M. Scherer, and P.G. Tratnyek. 1996. Kinetics of Halogenated Organic Compound Degradation by Iron Metal. *Environmental Science and Technology*, 30 (8), 2634-2640.

Köber, R., O. Schlicker, M. Ebert, and A. Dahmke. 2002. Degradation of Chlorinated Ethylenes by Fe^0: Inhibition Processes and Mineral Precipitation. *Environmental Geology*, 41, 644-652.

Li, L., C.H. Benson, and E.M. Lawson. 2005. Impact of Mineral Fouling on Hydraulic Behavior of Permeable Reactive Barriers. *Ground Water*, 43(4), 582-596.

Mackenzie, P.D., D.P. Horney, and T.M. Sivavec. 1999. Mineral Precipitation and Porosity Losses in Granular Iron Columns. *Journal of Hazardous Materials*, 68, 1-17.

Matheson, L.J., and P.G. Tratnyek. 1994. Reductive Dehalogenation of Chlorinated Methanes by Iron Metal. *Environmental Science and Technology*, 28 (12), 2045-2053.

Mayer, K.U. 1999. A Numerical Model for Multicomponent Reactive Transport in Variably Saturated Porous Media. Ph.D. Thesis, Department of Earth Sciences, University of Waterloo, Ontario, Canada, 286 pp.

Mayer, K.U., D.W. Blowes, and E.O. Frind. 2001. Reactive Transport Modeling of an In Situ Reactive Barrier for the Treatment of Hexavalent Chromium and Trichloroethylene in Groundwater. *Water Resources Research*, 37 (12), 3091-3103.

Mayer, K.U., D.W. Blowes, and E.O. Frind. 2002. Multicomponent reactive transport modeling in variably saturated porous media using a generalized formulation for kinetically controlled reactions. *Water Resources Research*, 38 (9), 1174, 13-1 – 13 - 21.

Nordstrom, D.K. 1977. Thermochemical Redox Equilibria of Zobell's Solution. *Geochimica et Cosmochimica Acta*, 41, 1835-1841.

O'Hannesin, S.F., and R.W. Gillham. 1998. Long-Term Performance of an In Situ "Iron Wall" for Remediation of VOCs. *Ground Water*, 36 (1), 164-170.

Orth, W. S., and R.W. Gillham. 1996. Dechlorination of Trichloroethene in Aqueous Solution Using Fe^0. *Environmental Science and Technology*, 30 (1), 66-71.

Phillips, D.H., B. Gu, D.B. Watson, Y. Roh, L. Liang, and S.Y. Lee. 2000. Performance Evaluation of a Zerovalent Iron Reactive Barrier: Mineralogical Characteristics. *Environmental Science and Technology*, 34 (19), 4169-4176.

Reardon, E.J. 1995. Anaerobic Corrosion of Granular Iron: Measurement and Interpretation of Hydrogen Evolution Rates. *Environmental Science and Technology*, 29 (12), 2936-2945.

Reardon, E.J. 2005. Zerovalent Irons: Styles of Corrosion and Inorganic Control on Hydrogen Pressure Buildup. *Environmental Science and Technology*, 39, 7311-7317.

Roh, Y., S.Y. Lee, and M.P. Elless. 2000. Characterization of Corrosion Products in the Permeable Reactive Barriers. *Environmental Geology*, 40 (1-2), 184-194.

Su, C., and R.W. Puls. 1999. Kinetics of Trichloroethene Reduction by Zerovalent Iron and Tin: Pretreatment Effect, Apparent Activation Energy, and Intermediate Products. *Environmental Science and Technology*, 33 (1), 163-168.

Tratnyek, P.G., T.L. Johnson, M.M. Scherer, and G.R. Eykholt. 1997. Remediating Ground Water with Zero-Valent Metals: Chemical Considerations in Barrier Design. *Ground Water Monitoring and Remediation*, 17 (4), 108-114.

U.S. Environmental Protection Agency. 1979. Analysis of Trihalomethanes in Drinking Water by Liquid-Liquid Extraction. Federal Register Vol. 44, No. 231:68683.

U.S. Environmental Protection Agency. 1982. Methods for Organic Chemical Analysis of Municipal and Industrial Wastewater. EPA-600/4-82-057.

U.S. Environmental Protection Agency, http://www.epa.gov/safewater/mcl.html (accessed June 2006).

VanStone, N.A., R.M. Focht, S.A. Mabury, and B.S. Lollar. 2004. Effects of Iron Type on Kinetics and Carbon Isotopic Enrichment of Chlorinated Ethylenes During Abiotic Reduction on Fe(0). *Ground Water*, 42 (2), 268-276.

Vogan, J.L., R.M. Focht, D.K. Clark, and S.L. Graham. 1999. Performance Evaluation of a Permeable Reactive Barrier for Remediation of Dissolved Chlorinated Solvents in Groundwater. *Journal of Hazardous Materials*, 68, 97-108.

Wolery, T.J., and S.A. Daveler. 1992. *EQ6, A Computer Program for Reaction Path Modeling of Aqueous Geochemical Systems: Theoretical Manual, User's Guide, and Related Documentation (version 7.0)*. E1.28: UCRL-MA-110662Pt4, Lawrence Livermore National Laboratory, Livermore, CA, 338 pp.

Yabusaki, S., K. Cantrell, B. Sass, and C. Steefel. 2001. Multicomponent Reactive Transport in an In Situ Zero-Valent Iron Cell. *Environmental Science and Technology*, 35 (7), 1493-1503.

Zhang, Y., and R.W. Gillham. 2005. Effects of Gas Generation and Precipitates on Performance of Fe^0 PRBs. *Ground Water*, 43 (1), 113-121.

Zobell, C. E. 1946. Studies on Redox Potential of Marine Sediments. *Bulletin of the American Association of Petroleum Geologists*, 30 (4), 477-513.